Doctoral Thesis

Establishment and Application of Diamond Detector Analysis System

Chidong Kong

Department of Nuclear Engineering

Graduate School of UNIST

2020

Establishment and Application of Diamond Detector Analysis System

Chidong Kong

Department of Nuclear Engineering
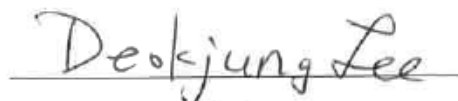
Graduate School of UNIST

Establishment and Application of Diamond Detector Analysis System

A thesis/dissertation

submitted to the Graduate School of UNIST

in partial fulfillment of the

requirements for the degree of

Doctor of Philosophy

Chidong Kong

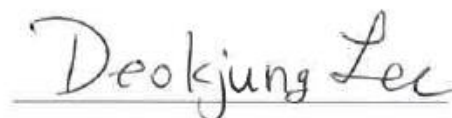January 7, 2020

Approved by

Deokjung Lee

Advisor

Deokjung Lee

Establishment and Application of Diamond Detector Analysis System

Chidong Kong

This certifies that the thesis/dissertation of Chidong Kong is approved.

January 7, 2020

Advisor: Deokjung Lee

Dong-Seong SOHN

Eisung Yoon

Chang Je Park

Hyun Chul Lee

Contents

List of Figures

List of Tables

Abstract

In this study, a diamond detector in a mixed neutron-photon field of the CROCUS research reactor at École Polytechnique Fédérale de Lausanne (EPFL) is modeled. Simulations are carried out to analyze pulses from the diamond detector in more detail, which induce a novel discovery. Through a code-to-code comparison, the Monte Carlo codes SERPENT v2.1.29 and GEANT4 v10.04.p02 are selected for the CROCUS whole core calculation and the detailed physics modeling in the diamond crystal, respectively. The neutron and prompt gamma ray contributions to the detector are modeled by a two-step procedure (SERPENT2/GEANT4), and the simulation of the delayed gamma ray contribution is carried out by a three-step procedure (SERPENT2/STREAM-SNF/GEANT4). The simulations show that the fraction of the gamma-to-neutron fluxes in the diamond detector is approximately 91.4%, and that of the delayed-to-prompt gamma fluxes is approximately 47.2%.

By using the flux spectra calculated at the location of the detector, the physics of particle interactions with the diamond crystal is investigated. The contributions of the neutrons and gamma rays to the diamond detector signal amount to approximately 27% and 73%, respectively. The energies and positions of the particles contributing to the detector signal as tallied in GEANT4 are employed to reconstruct numerical pulses and create a scatter plot. In the scatter plot, pulses are arranged according to the energy for each calculation width, which is defined as the width at 0% of the maximum amplitude. The proton recoil plot shows two bands, one due to protons impacting the anode and the other by protons impacting the cathode, thus showing that protons do not have sufficient energy to penetrate the diamond crystal and have the same probability of interacting with the anode and cathode. This tendency also appears as a high-energy tail in a pulse energy spectrum consisting of the number of pulses according

to the energy distribution. Meanwhile, neutron scattering collisions have a homogeneous distribution in the crystal. Hence, a structure with a higher count at the ballistic center region (BCR) is observed and is probably related to the amplitude of the BCR pulses being higher. Thus, it is possible to observe better pulses resulting from the energy depositions at the BCR.

Finally, the modeling performance is assessed by comparing the calculated results with the experimental data. In the pulse energy spectrum, a curve produced by the simulations matches with that produced by the measurements. The slope of the curves between 1 MeV and 2 MeV is mainly produced by gamma interactions. The high-energy tail is produced by neutron interactions, especially, the proton recoil. The lithium converter reactions in the diamond detector account for 14.31% and 15.13% beyond 1.34 MeV for the measurement and simulation, respectively, showing consistency.

Key words: Physical interaction, diamond crystal, diamond detector, Monte Carlo code, CROCUS, delayed gamma, particle interaction.

I.   Introduction

I.1. Background

Diamond detectors are considered suitable for use in nuclear reactors owing to their fast response time, strong durability against radiation, and capability to acquire a wide energy spectrum from 0 to 14 MeV, with the additional advantage that gamma rays and thermal/fast neutrons are measurable and distinguishable [1,2]. In previous studies, measurements were performed using a diamond detector in the CROCUS research reactor to analyze the properties (type and energy) of the particles incident on the detector [3] using different pulsed patterns [2]. However, these experimental studies were limited to qualitative output because the contributions of the fast neutrons could not be distinguished at the time.

For example, **Fig. 1** shows a scatter plot of the signals acquired from a diamond detector in the CROCUS reactor. In **Fig. 1**, "cps" is counts per second and is indicated by a log scale. The signals are sorted by width at 12.5% of the maximum and by energy. Horizontal structures at widths of 5, 7, and 10 ns can be observed as reported by Hursin et al. [3]. The 7 and 10 ns structures represent the drift of electrons and holes generated by interactions near the anode and cathode, respectively. The 5 ns structure represents the drift of the secondary ions generated by the scattering of gamma rays and fast neutrons in the diamond crystal. For this 5 ns structure, the effects of the gamma rays and those of the fast neutrons are difficult to distinguish because of the deformation of the fast-neutron-induced pulse shape caused by the resistor-capacitor (RC) constant.
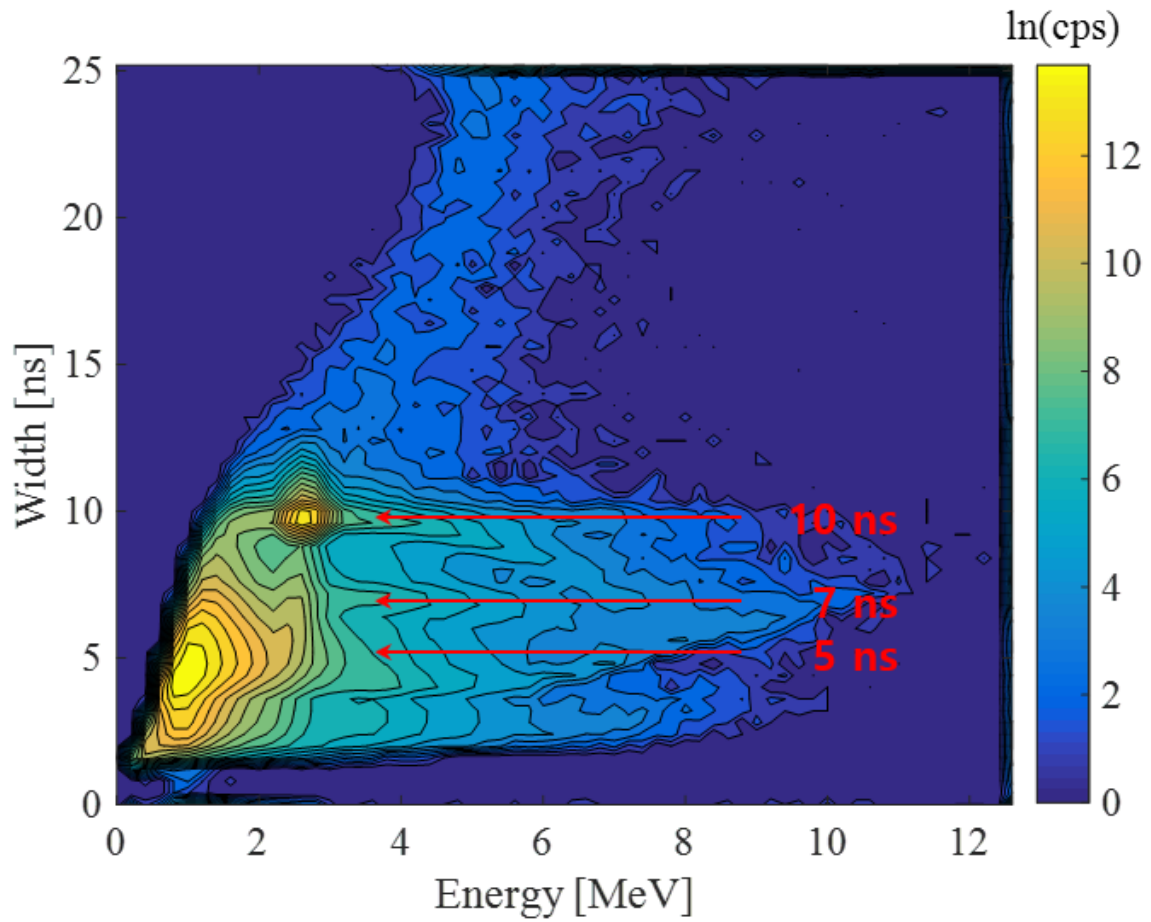
Fig. I-1. Scatter plot of signals acquired from a diamond detector in the CROCUS research reactor sorted by width at 12.5% of the maximum and by energy.

I.2. Objective of Thesis

This study aims to understand the effect of a mixed field of neutrons and gamma rays on the response of a diamond detector located in the CROCUS reactor through modeling. Several simulations are performed to tackle the analysis of the several different contributions to the detector signal. The contributions of the neutrons and prompt gamma rays are determined by a two-step procedure: (1) SERPENT2 neutron-photon simulation [4] of the whole CROCUS core ("global" simulations) to obtain the CROCUS neutron and prompt gamma spectra at the locations of interest, and (2) GEANT4 simulation [5] of the diamond detector ("local" simulations using the fluxes calculated during the global simulation as input) to simulate the detailed transport of diverse particles (i.e., neutrons, gamma rays, electrons, heavy ions, etc.) at the level of the detector. For the contribution from the delayed activation gamma, an additional step with the STREAM-SNF code [6,7] is added in the two-step procedure previously described, resulting in a SERPENT2/STREAM-SNF/GEANT4 three-step procedure [4-7]. The SERPENT2 code is chosen for the global simulations to take advantage of the fast calculation speed in terms of a burnup calculation. The GEANT4 code is chosen for local simulation to take advantage of its detailed charged particle transport physics, especially heavy ion interactions that are not simulated by SERPENT2. Because SERPENT2 does not provide a gamma source rate, the STREAM-SNF code is adopted for the source-term calculation.

The remainder of this paper is organized as follows. Chapter II describes the experimental facilities in École Polytechnique Fédérale de Lausanne (EPFL), that is, the CROCUS research reactor, NEUTRON detection system, and diamond detector. Chapter III shows the preliminary analysis and code verification results. In this chapter, charged pulses are

shown as an example. Chapter IV details the modeling of the neutron, the prompt and delayed gamma ray contributions to the signal of the diamond detector in a mixed CROCUS neutron-photon field. Chapter V presents a phenomenological assessment of the particle interaction physics in the diamond detector with a pulse energy spectrum and a scatter plot, and it investigates the contributions of the gamma rays, and fast and thermal neutrons to the detector signal. Neutron count signals depending on the energy and position of the incident particles are also shown. Chapter VI compares the calculated detector results with the experimental data acquired in CROCUS. Finally, Chapter VII describes the conclusions derived from the results and discusses perspectives for further study.

II. Experimental Facility for Validation

II.1. Water tank CARROUSEL

A water tank CARROUSEL comprises a Pu-Be neutron source at the center and a BF_3 detector or ^{3}He detector besides the neutron source.

Fig. II-1 shows the water tank. The radius of the water tank is 75.3 cm, and the height is 160 cm. The distance between the neutron source and the detector is 50 cm.
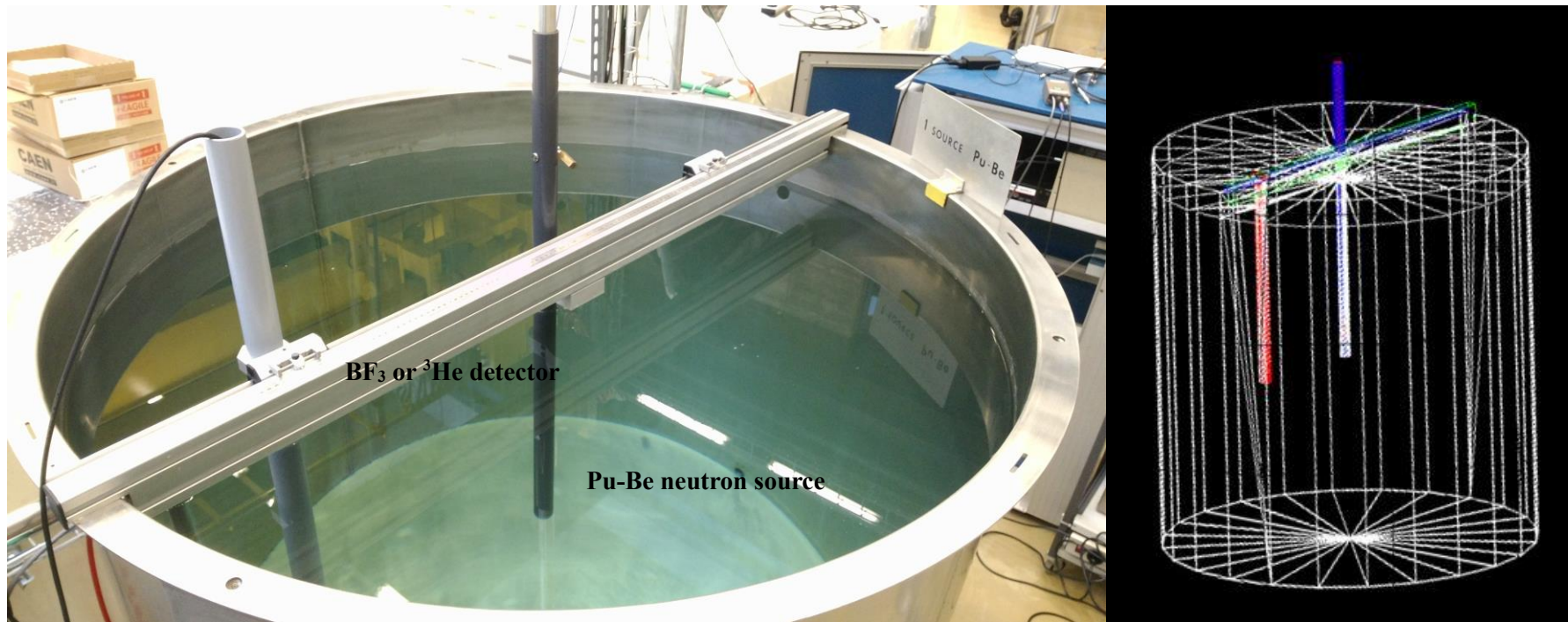
Fig. II-1. Water tank CARROUSEL (left), CARROUSEL plotted by GEANT4 (right).

II.2. Zero-power CROCUS research reactor

CROCUS is a zero-power research reactor with maximum power of 100 W (regulatory limit). The CROCUS reactor comprises two zones: a central region with 2% enriched UO_2 fuel surrounded by a region with 1% enriched U-metal fuel. The diameter and height of the CROCUS active core are 58 cm and 100 cm, respectively. **Fig. II-2** shows the experimental configuration of CROCUS with the location of the diamond detector.

During the experiment, the diamond detector was installed in the guide tube of the south–east control rod as shown in **Fig. II-2**. In the top view of **Fig. II-2**, the green area between the U-metal fuel and water is a cadmium layer consisting of natural cadmium. The orange region below and above the core in the front view is air consisting of nitrogen (~79%) and oxygen (~21%). The dark blue region is a support material consisting of natural aluminum. The axial position of the diamond detector in the core is fixed at 50 cm from the upper grid plate marked with dark blue in the front view, that is, the diamond detector is centered on the axial mid-plane of the active core where the neutron flux is maximum in the axial direction. The CROCUS fuel is considered always fresh because of the low power [8].

Top View   Front View
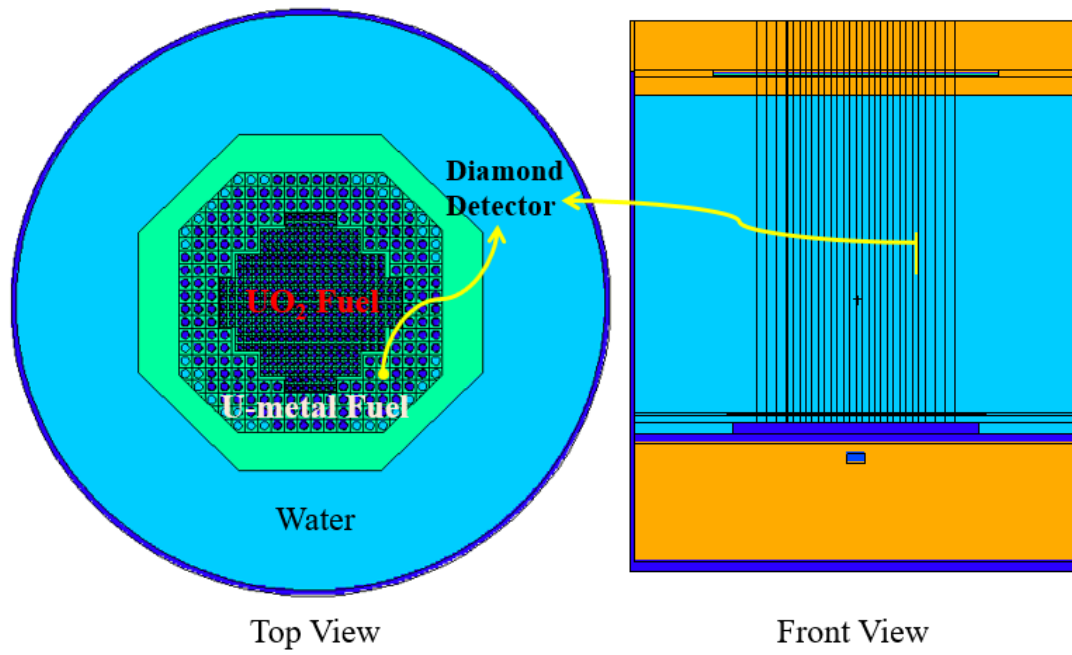
Fig. II-2. Configuration of zero power CROCUS research reactor.

II.3. NEUTRON detection system

The NEUTRON detection system is composed of a CIVIDEC C2 Broadband Amplifier, a ROSY AX106 readout system, and the single-crystal chemical vapor deposition (sCVD) diamond detector.

Signals are transferred to the readout system from the sCVD diamond detector. The readout system analyzes the detector signals with a sampling rate of 5 giga-samples/s, eight-bit ADC resolution, and a bandwidth of 250 MHz. The amplitude, full width at half maximum (FWHM), and energies of the pulses are recorded online by the readout system.

II.4. Diamond detector

Fig. II-3 shows the geometry of the sCVD diamond detector employed in CROCUS. The diamond detector comprises four parts: (1) a ^{6}LiF converter, (2) a polyethylene collimator and a holder, (3) an anode and a cathode, and (4) the diamond crystal. In **Fig. II-3**, the ^{6}LiF converter, diamond crystal, collimator, and holder are box-shaped. The dimensions of the ^{6}LiF converter, diamond crystal, and collimator and holder are 0.4 cm × 0.4 cm × 1.8 μm, 0.4 cm × 0.4 cm × 500 μm, and 2 cm × 2 cm × 1.6 mm, respectively. There is a circular air hole with a radius of 0.15 cm between the ^{6}LiF converter and diamond crystal. Across the diamond crystal, a voltage of 400 V is applied to collect the electrons and holes generated by ionization in the diamond crystal. The purpose of the ^{6}LiF converter is to convert incident thermal neutrons into alpha and triton particles through a (n,α) reaction with the ^{6}Li atoms (large cross section in the thermal domain, about 940 barns for neutrons of 0.0253 eV energy), whereas most fast neutrons pass through the ^{6}LiF converter without interactions. The alpha and triton particles produced in the converter then interact with the diamond instantly after passing the air gap, thus producing rectangular pulses, whereas the fast neutrons interacting in the diamond crystal produce step-like pulses.
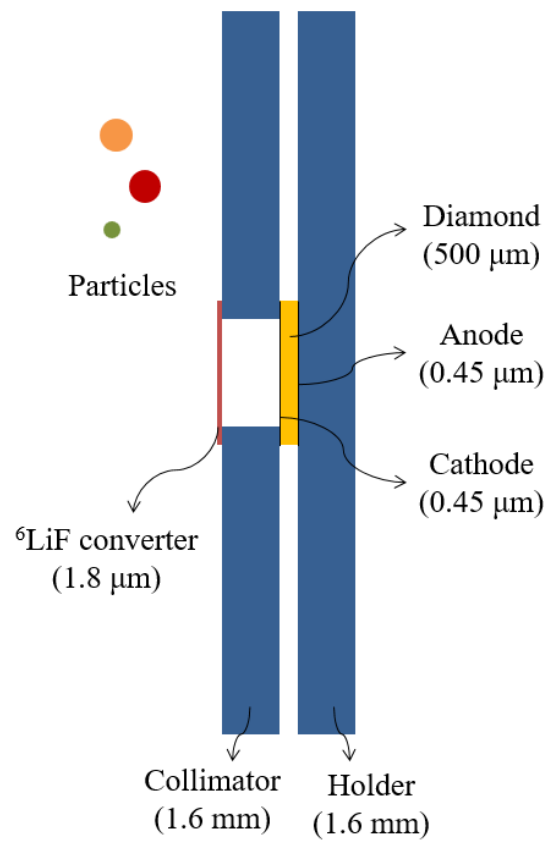
Fig. II-3. Configuration of sCVD diamond detector.

III. Preliminary Analysis and Code Validation/Verification

In Chapter III, the three Monte Carlo codes, MCNP6, SERPENT v2.1.29 and GEANT4 [4,5,9], are compared with each other for code verification and validation.

III.1. Ionization profile in the diamond crystal

Before discussing the preliminary results of the diamond detector modeling, this section describes the characteristics of the diamond detector with real charge collection pulse examples. When ionization occurs in the diamond crystal, an electron-hole pair is created, and the electron moves to the anode and the hole moves to the cathode. The ballistic center (BCR) of the diamond crystal is defined as the location where the drift time of the electron to the anode and of the hole to the cathode is equal. For example, if the velocity of the electrons in the crystal is 40 μm/ns and the velocity of the holes is 60 μm/ns, the BCR will be located 200 μm from the anode and 300 μm from the cathode for a 500-μm thick diamond crystal. According to the Shockley–Ramo theorem, different signal shapes are produced depending on the ionization profile in the diamond detector [1,2]:

- A rectangular signal shape is produced when an alpha or a triton particle causes a point-like ionization at the cathode. These particles are generated by the interaction between a thermal neutron and a ^{6}Li atom of the lithium converter. The alpha or triton particle produced in the converter interacts with the diamond crystal instantly after passing the air gap, thus producing a rectangular pulse. Since the hole drift time at the cathode vicinity is too short to be detected, this pulse represents only electron drift.

- A rectangular signal shape is produced when a point-like ionization occurs at the BCR of the diamond crystal.

14

- A step-like signal shape is produced when a point-like ionization occurs in the diamond crystal elsewhere other than the BCR. The electron and hole generated by ionization produce rectangular pulses each, with the amplitude inversely proportional to their respective drift time owing to charge conservation. Consequently, the final current signal is the superposition of the two rectangular pulses. Depending on where the ionization occurs, the effect of the electron or of the hole may be greater than the other. In actual measurements, step-like pulses can appear rectangular when the ionization occurs near the electrodes because of the effect of RC time.

- A triangular signal is produced when an ionizing particle (for instance, a Compton electron) travels in the diamond crystal. This particle causes secondary ionizations homogeneously as it moves to the anode and triangular pulses result from the free charge carriers that are continuously absorbed into the electrodes while the remaining charges are moving. In other words, the triangular pulses are generated by the superposition of many drifts of homogeneous secondary products (i.e., electrons and holes). **Fig. III-1** shows an example of the charge collection pulses.
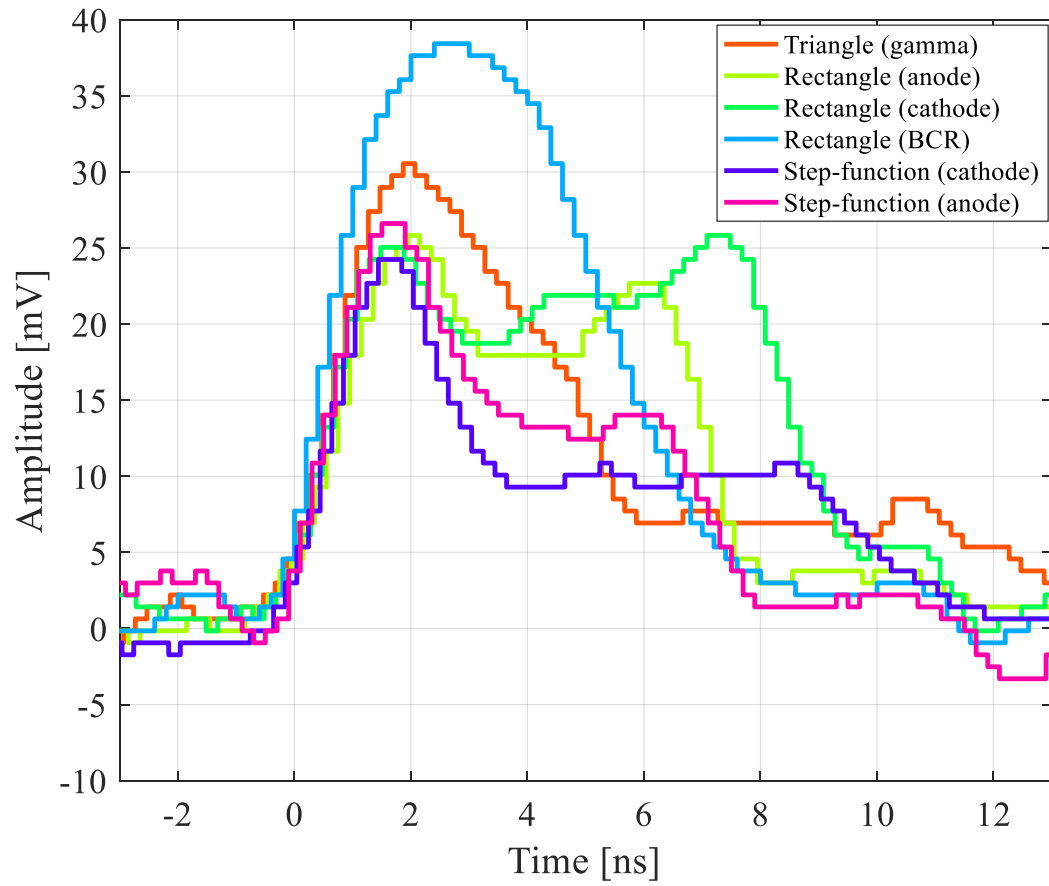
Fig. III-1. Real example of charge collection pulse from the diamond detector.

A charge collection pulse means the electrical signal generated by the drifts of electrons and holes with zero seconds when a reaction occurs inside the diamond crystal. When the RC time constant of the electron chain can be ignored, the rectangular pulses produced from the BCR can theoretically be distinguished from the triangular pulses produced by the gamma interactions. This distinction is difficult in practice as illustrated in **Fig. III-1**, which show that the rectangular pulse generated at the BCR looks similar to the triangular pulse caused by the effect of the RC constant. The rectangular pulse is not perfect owing to the space charge effect.

III.2. Code-to-code comparison for diamond response in a mixed radiation field

The code-to-code comparison for diamond response was performed to determine which code is suitable for the physics modeling in the diamond crystal. In 2016, Weiss *et al.* [1] published the energy deposition spectrum in a diamond crystal irradiated with a 14.3 MeV neutron source as calculated with GEANT4 v09.06.p02. This calculation is reproduced in this paper with GEANT4 v09.06.p02, a newer version of GEANT4 (GEANT4 v10.04.p02) and MCNP6 [9]. The calculated results are compared in **Fig. III-2**.
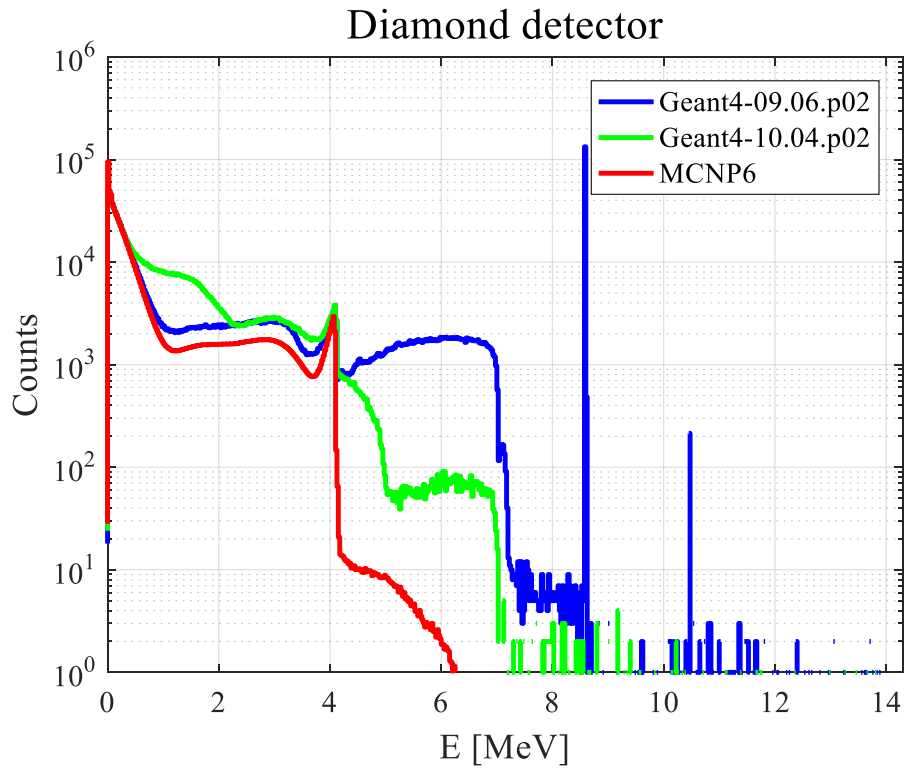
Fig. III-2. Simulated energy deposition spectrum in the diamond crystal irradiated with

a 14.3 MeV neutron source.

The GEANT4 v09.06.p02 results presented in **Fig. III-2** are consistent with the results presented in Weiss *et al.* [1]. GEANT4 v10.04.p02 and GEANT4 v09.06.p02 use different neutron libraries (v10 uses G4NDL4.5 and v09 uses G4NDL4.2) that model the neutron inelastic scattering contribution differently, thus causing the results to be different between v09 and v10. SERPENT v2.1.29 does not have a function for tracking heavy ions and electrons and a tally capacity of energies deposited by neutrons; thereby it is considered not suitable for various interactions in the diamond crystal. (The function for tallying energies deposited by neutrons has been added to SERPENT v2.1.31.) MCNP6 is the Monte Carlo code known as a tracking function of more particles than SERPENT2. However, in the MCNP6 results, all the inelastic responses above 4 MeV, *i.e.*, ^{12}C(n,n+2α)α, ^{12}C(n,α)^{9}Be, ^{13}C(n,α)^{10}Be, are missing because MCNP6 cannot transport particles with mass greater than α particles [10]. This is a severe limitation for the detailed simulation of the neutron response in the diamond crystal because it neglects, for instance, the contribution from ^{9}Be ions generated from the reaction ^{12}C(n,α)^{9}Be from neutrons of energies of 7.2 MeV or greater.

$$
\begin{aligned}
n + {}^{12}C \rightarrow n' + {}^{12}C^{*} \rightarrow \alpha + {}^{8}Be \rightarrow 2\alpha, \\
n + {}^{12}C \rightarrow \alpha + {}^{9}Be^{*} \rightarrow n' + {}^{8}Be \rightarrow 2\alpha.
\end{aligned}
\tag{1}
$$
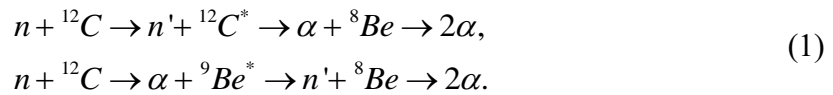
Eq. (1) shows how three alpha particles are produced by ^{12}C(n,n+2α)α reactions [11]. In Eq. (1), *n* corresponds to a neutron, *n'* indicates a neutron that lost energy due to an inelastic collision, and * indicates an excited state. GEANT4 deals with these reactions using a multi-step breakup model ported from the NRESP7.1 Monte Carlo code developed by Physikalisch-Technische Bundesanstalt (PTB) [12]. SERPENT2 and MCNP6 have a limitation in handling these reactions because they cannot transport particles beyond the mass number of the α particle.

III.3. Modeling the neutron response of BF$_3$ and ^{3}He detectors

A BF$_3$ detector detects neutrons in the principle shown in Eq. (2).

$$n + {}^{10}B \rightarrow {}^{4}He \ (1.47 \ \text{MeV}) + {}^{7}Li^{*} \ (0.84 \ \text{MeV}) \quad (94\% \ \text{of the total reactions}),$$
$$n + {}^{10}B \rightarrow {}^{4}He \ (1.78 \ \text{MeV}) + {}^{7}Li \ (1.02 \ \text{MeV}) \quad (\ 6\% \ \text{of the total reactions}). \tag{2}$$
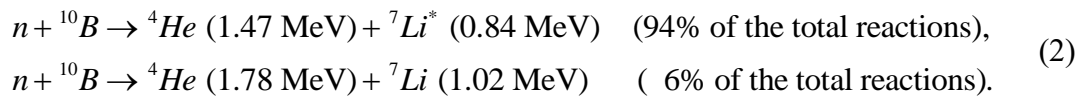
In Eq. (2), thermal neutrons are absorbed to a ^{10}B atom of BF$_3$ gas particles and emit
^{4}He (alpha) and ^{7}Li particles. At this point, the energy of the neutrons is negligible, and the
energies of ^{4}He and ^{7}Li particles are already set. With a 94% probability, the ^{4}He and ^{7}Li
particles have energies of 1.47 MeV and 0.84 MeV, respectively, and with a 6% probability,
they have energies of 1.78 MeV and 1.02 MeV, respectively. The ^{4}He and ^{7}Li particles pass
through and transmit their energy to the BF$_3$ gas medium.

However, if the (n,^{10}B) reaction takes place in a border of the BF$_3$ gas medium, one of
the emitted particles cannot fully transmit its energy to the medium. Because the ^{4}He or ^{7}Li
particle transmit only part of its energy to the medium, the total energy deposited in the medium
is smaller than the emitted one. This phenomenon is called the wall effect.

For example, as shown in **Fig. III-3**, suppose the (n,^{10}B) reaction produces two particles
(^{7}Li with energy of 0.84 MeV and ^{4}He with energy of 1.47 MeV) at the border of a detector.
Assume that the ^{7}Li particle faces toward the center of the detector, while the ^{4}He particle faces
outside the detector, the ^{7}Li particle transmits its full energy to the medium, whereas the ^{4}He
particle transmits only 0.2 MeV out of 1.47 MeV to the medium. Subsequently, the total energy
recorded by the detector is 1.04 MeV, not 2.31 MeV. In this manner, some reactions have

energies between the maximum and minimum emission energies. (For the BF_3 detector, the maximum energy is 2.31 MeV and the minimum is 0.84 MeV.)

Similarly, the same principle can be applied to a ^{3}He detector.

$$n + {}^3He \rightarrow {}^1H \ (0.57 \text{ MeV}) + {}^3H \ (0.2 \text{ MeV}) \qquad (100\% \text{ of the total reactions}). \qquad (3)$$
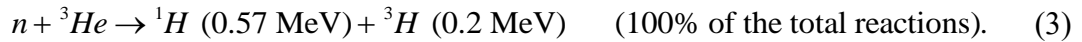
In Eq. (3), thermal neutrons are absorbed to a ^{3}He atom and emit ^{1}H and ^{3}H particles. At this point, the energy of the neutrons is negligible, and the ^{1}H and ^{3}H particles have energies of 0.57 MeV and 0.2 MeV, respectively. The ^{1}H and ^{3}H particles pass through and transmit their energy to the ^{3}He gas medium. One of them transmits only part of its energy to the medium when the (n,^{3}He) reaction occurs in the border. The total energy deposited in the medium has a uniform distribution between the maximum and minimum emission energies. (For the ^{3}He detector, the maximum energy is 0.77 MeV and the minimum is 0.2 MeV.)
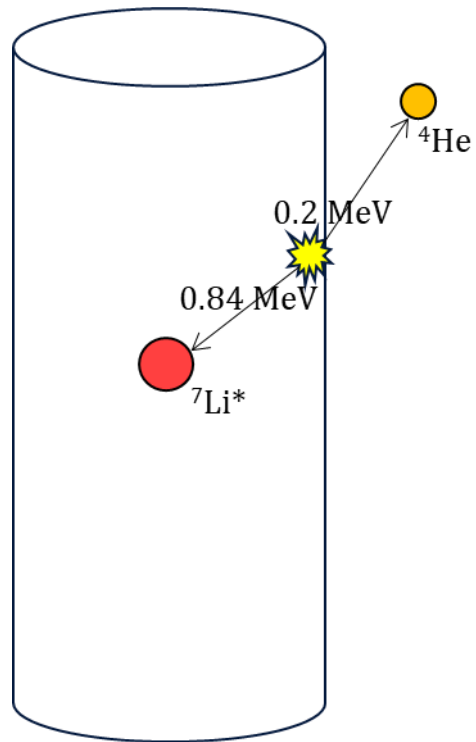
Fig. III-3. Principle of wall effect.

Before modeling the water tank CARROUSEL, a virtual detector with a radius of 1 cm and height of 20 cm is made by MCNP6 and GEANT4, respectively [4,5]. **Fig. III-4** shows the energy deposited in the BF_3 and ^3He detectors. The case "n(E)=0.0253 eV" indicates that only neutrons with an energy of 0.0253 eV are inserted into the detectors. Similarly, the case "n(E)=PWR Spectrum" means that neutrons that have a typical pressurized water reactor (PWR) spectrum are inserted into the detectors.

In **Fig. III-4**, MCNP6 and GEANT4 provide the same results. **Fig. III-4** shows that the orange and blue lines match well. First, the orange and blue lines show a step-like shape, which is seen as the count increasing one step from 0.84 MeV and another step from 1.47 MeV. This is a superposition of the uniform distribution at 0.84 ~ 2.31 MeV with the uniform distribution at 1.47 ~ 2.31 MeV. The uniform distribution at 0.84 ~ 2.31 MeV is formed because of the emission of the ^4He particles, and that at 1.47 ~ 2.31 MeV is generated because of the emission of the ^7Li particles.

By comparing the blue and yellow lines, the effect of the neutron spectrum on the wall effect can be identified. The overall shape of the yellow line is the same as that of the blue line; however, its magnitude is much smaller. This is because thermal neutrons react with ^{10}B atoms more actively. In contrast, reactions releasing more an energy more than 2.8 MeV are found in the yellow line. These reactions are from collisions between the fast neutrons and ^{10}B atoms, which means that the additional energy over 2.8 MeV comes from high-energy neutrons.

The sky-blue and red lines also matched well. The step-like shape of the wall effect is not clearly seen, which is caused by the short radius of the ^3He detector. Unlike the ^4He and ^7Li particles, the ^1H and ^3H particles are emitted with less energy. This means the mean-free path

of the ^{1}H and ^{3}H particles is longer than that of the ^{4}He and ^{7}Li particles. For the BF$_3$ detector, the ^{4}He and ^{7}Li particles born near the center of the detector transmit their full energy to the medium. However, for ^{3}He detector, the ^{1}H and ^{3}H particles born near the center of the detector have a higher possibility not to transmit their full energy even though the location of the reaction is same. In terms of the neutron energy spectrum, the same tendency as that of the BF$_3$ detector is observed.
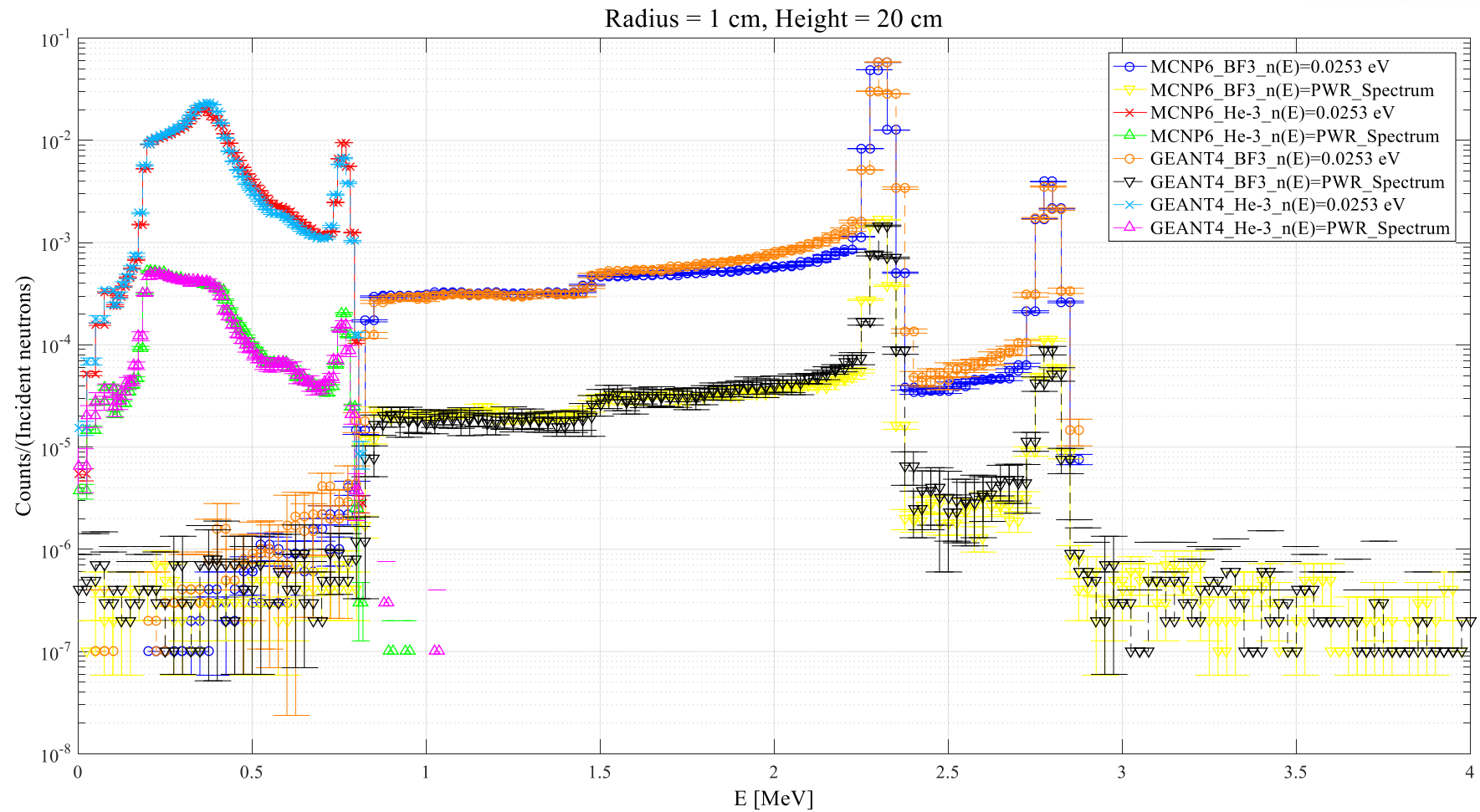
Fig. III-4. Energy deposition in BF$_3$ and ^{3}He detectors (Radius = 1 cm and Height = 20 cm).

Fig. III-5 shows the energy deposited in large BF_3 and ^{3}He detectors with radius of 3 cm. The same trends are observed as those in **Fig. III-5**. One noticeable change is the fact that the wall effect shape in the ^{3}He detector is changed to a stair shape. This is because the mean-free path of the ^{1}H and ^{3}H particles is smaller than the diameter of the detector.
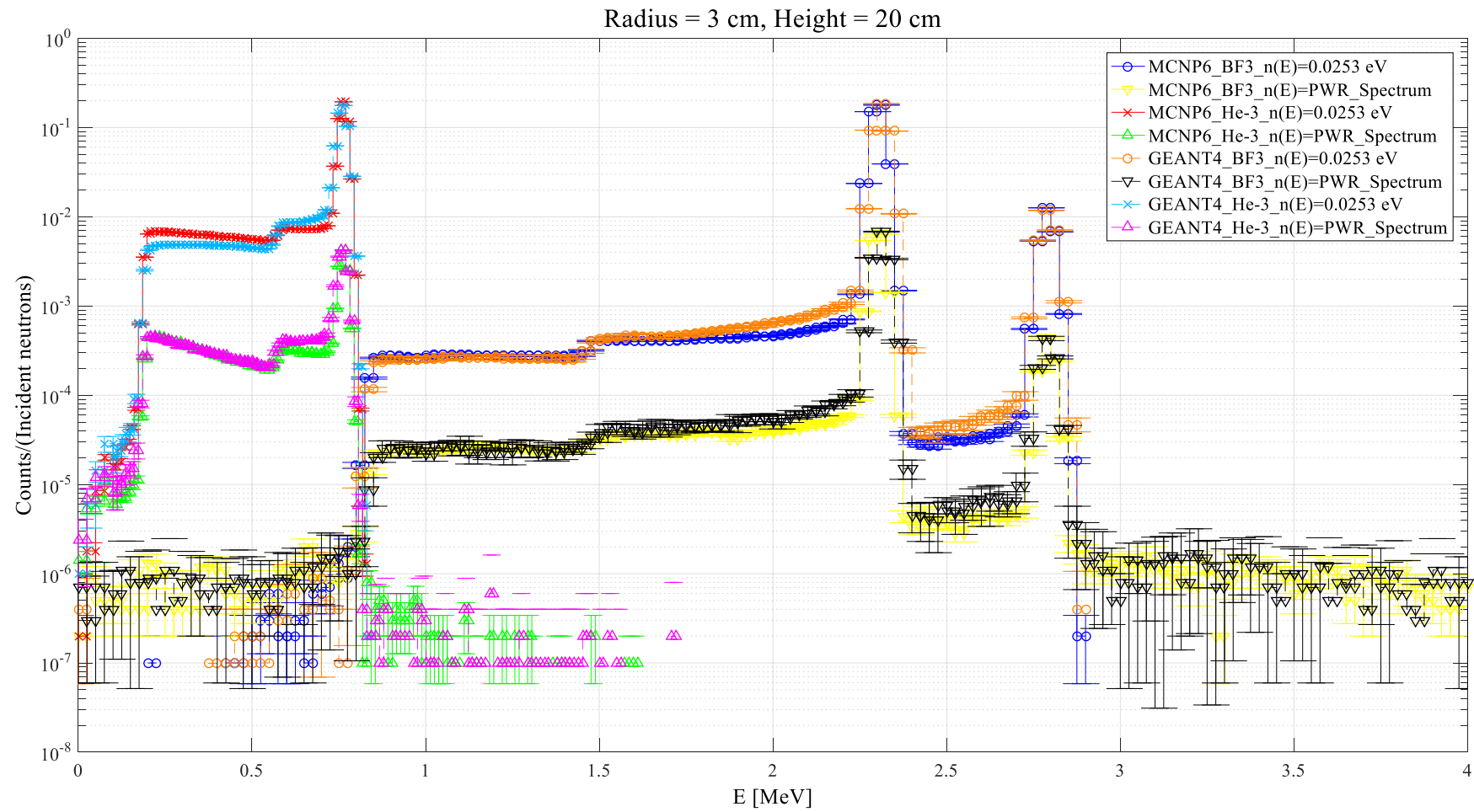
Fig. III-5. Energy deposition in BF$_3$ and ^{3}He detectors (Radius = 3 cm and Height = 20 cm).
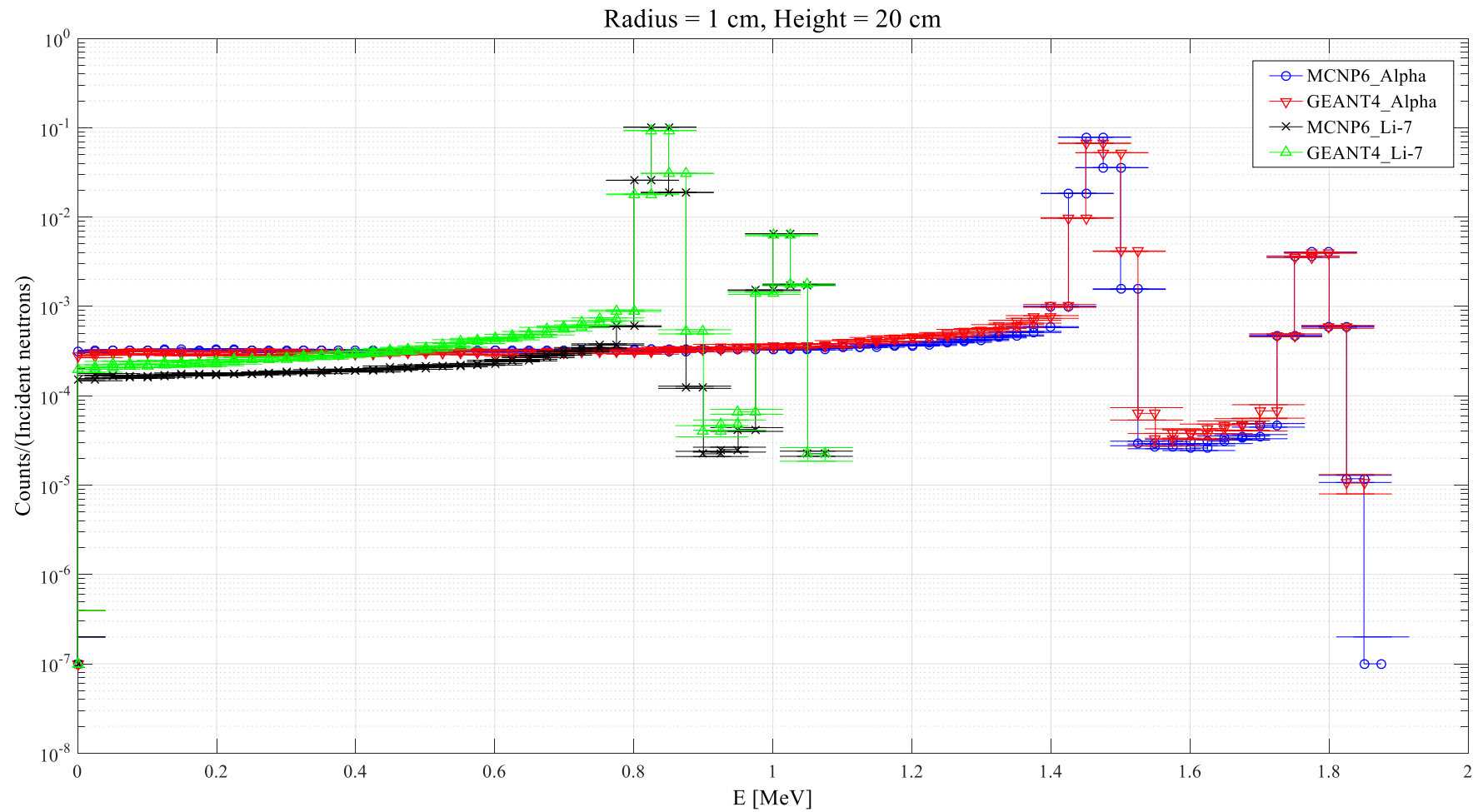
Fig. III-6. Energy deposition of alpha and ^{7}Li in BF$_3$ detector (Radius = 1 cm and Height = 20 cm).
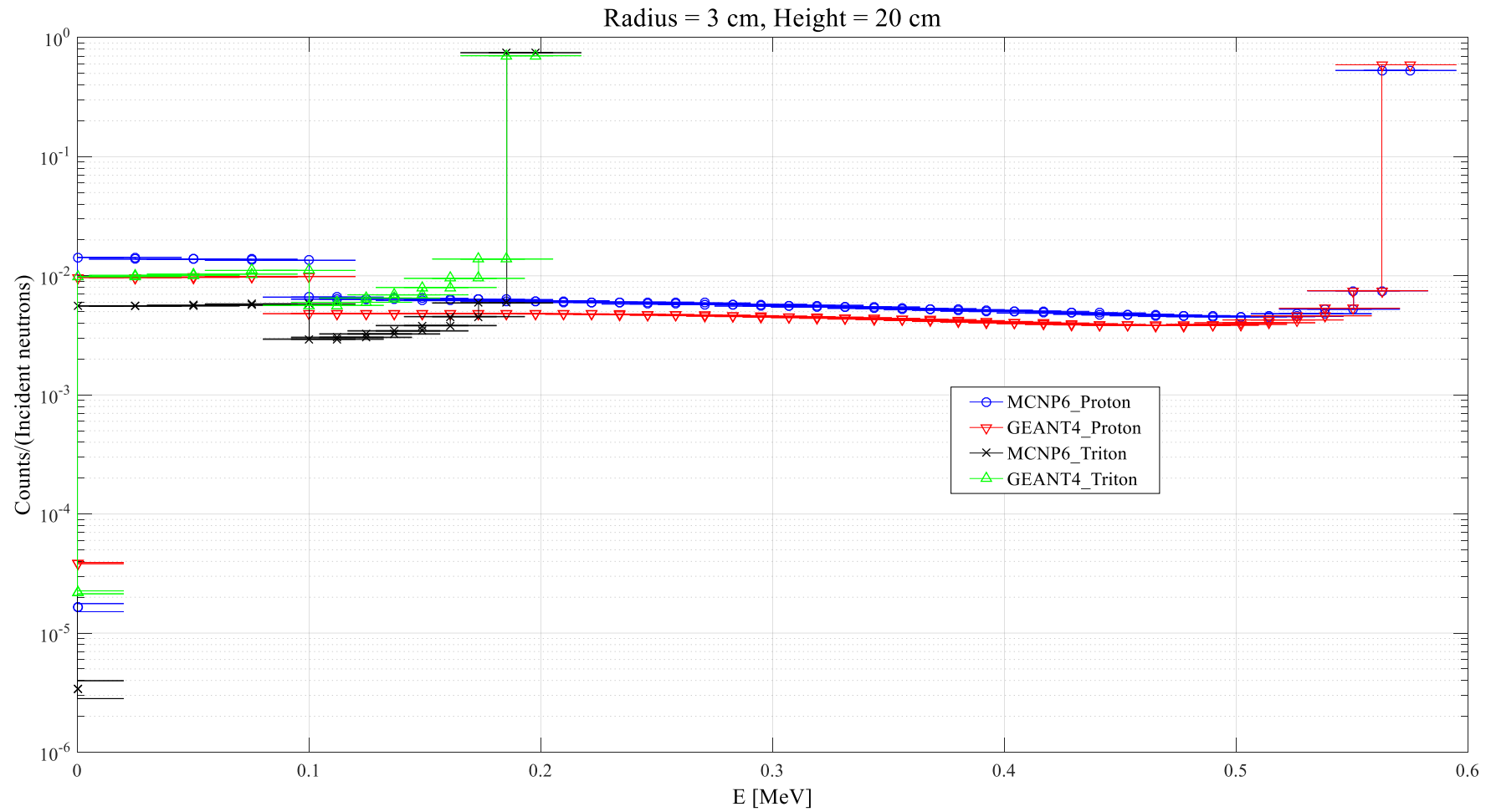
Fig. III-7. Energy deposition of proton and triton in ^{3}He detector (Radius = 3 cm and Height = 20 cm).
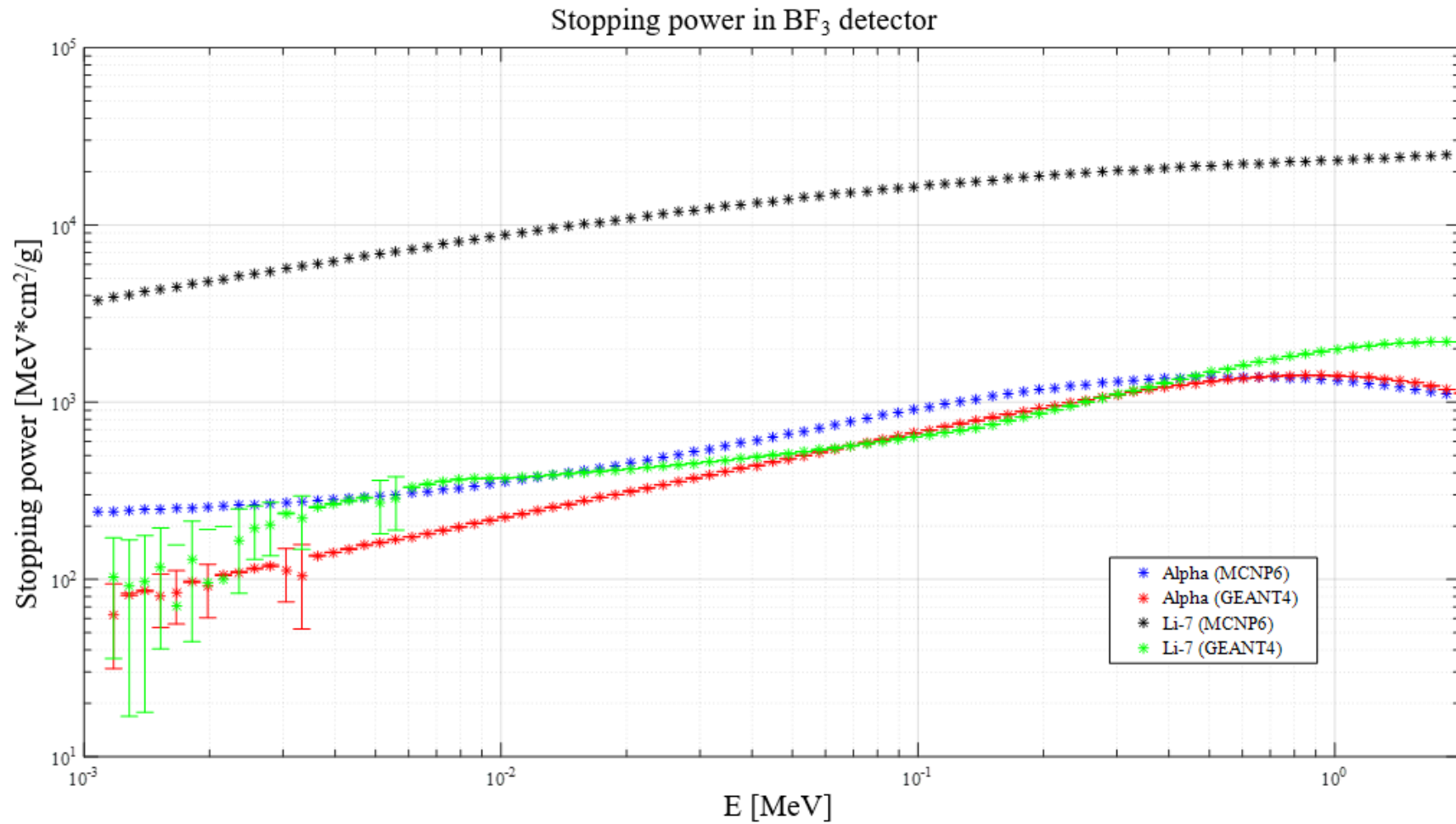
Fig. III-8. Stopping power of alpha and ^{7}Li in BF$_3$ detector.
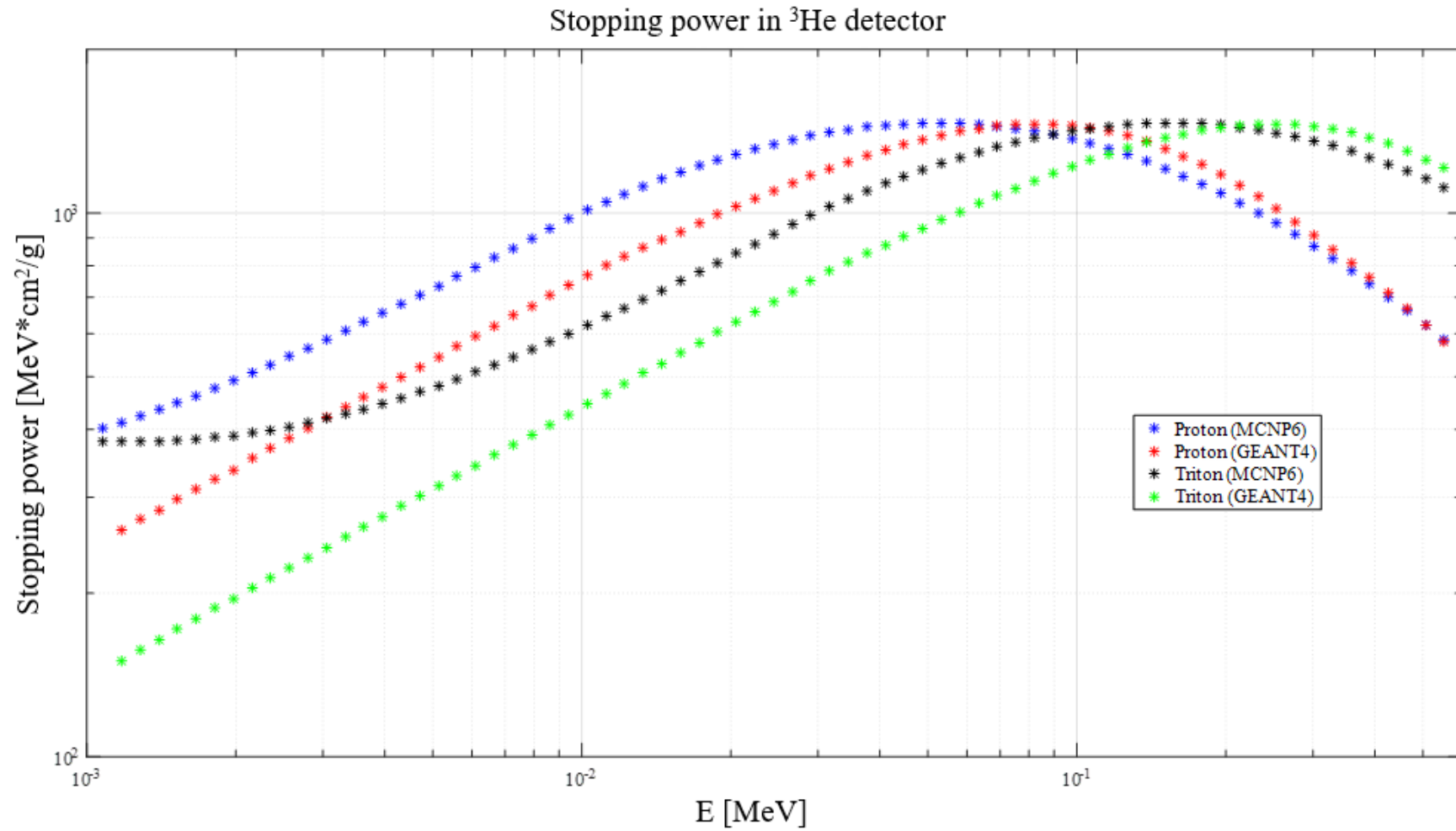
Fig. III-9. Stopping power of proton and triton in ³He detector.
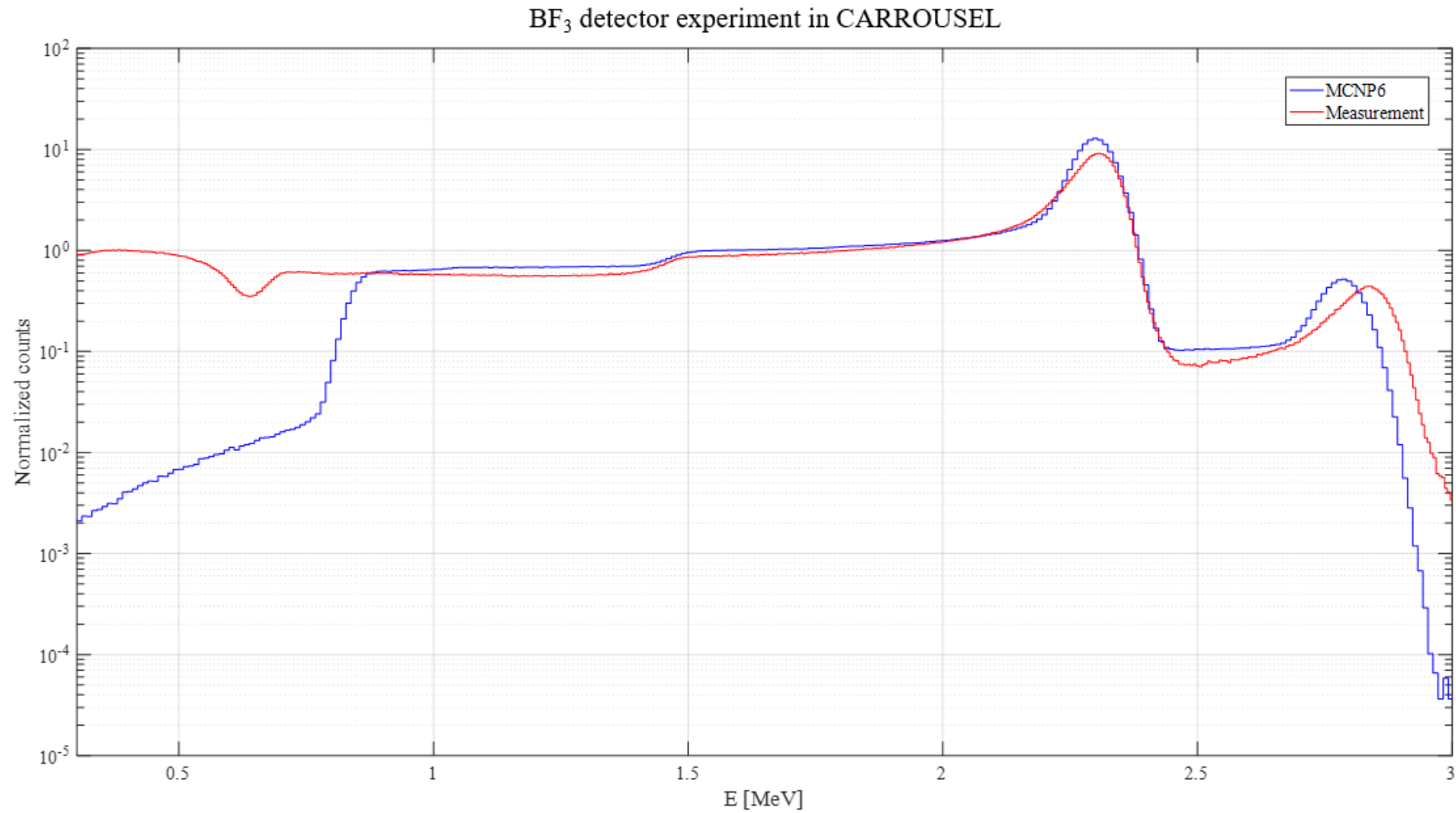
Fig. III-10. MCNP6 modeling and experimental results for BF$_3$ detector.
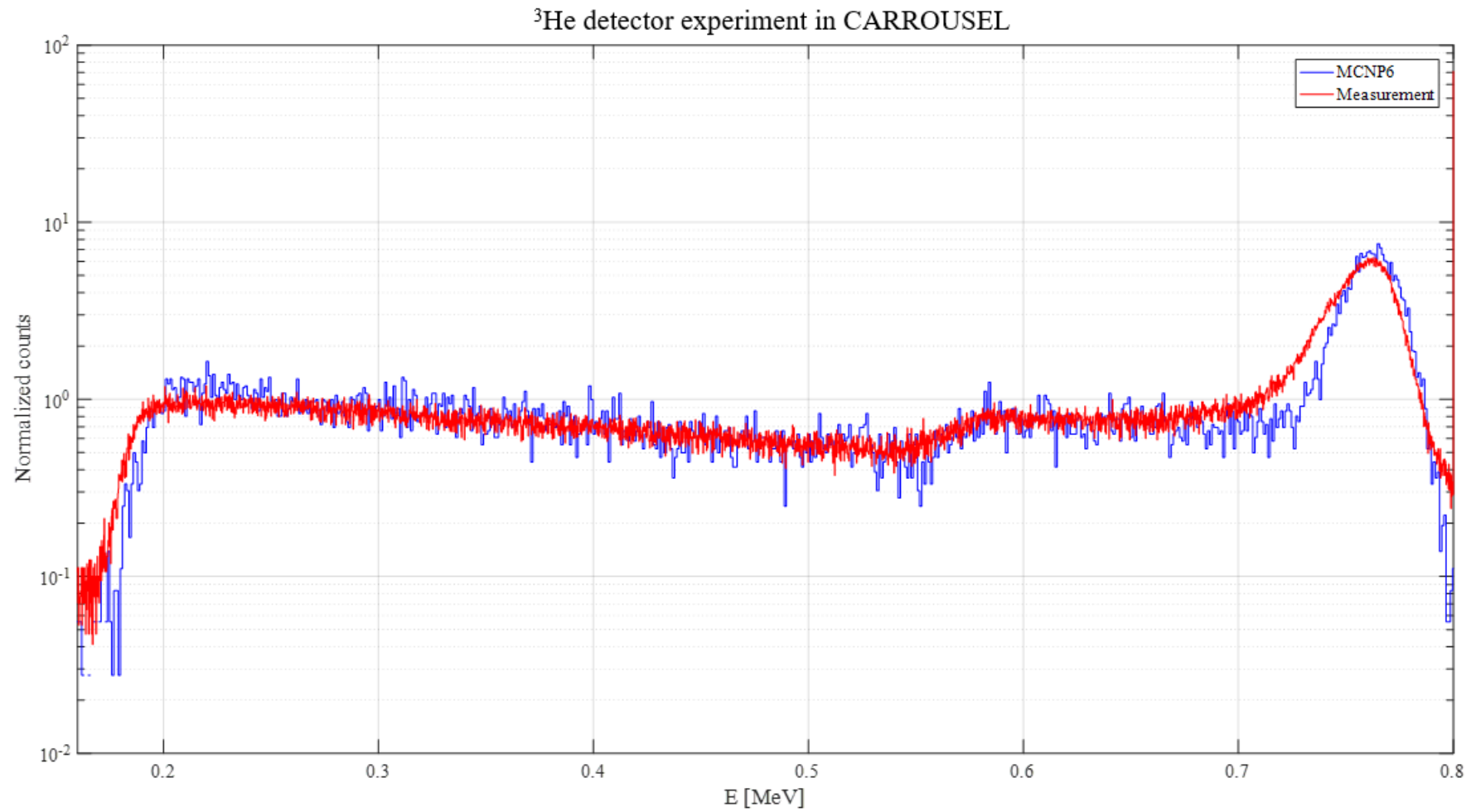
Fig. III-11. MCNP6 modeling and experimental results for ^{3}He detector.

III.4. Modeling of gamma ray response of a sodium iodide detector

The gamma spectrum was also validated. **Fig. III-12** shows a gamma-ray detection problem composed of an NaI detector (green color), a ^{60}Co gamma ray source (white dot), lead (blue color), and air (red color). The NaI detector is a 4-cm high cylinder and has a 2.85 cm radius with a density of 3.67 g/cm^3. The air is composed of 21% oxygen and 79% nitrogen.
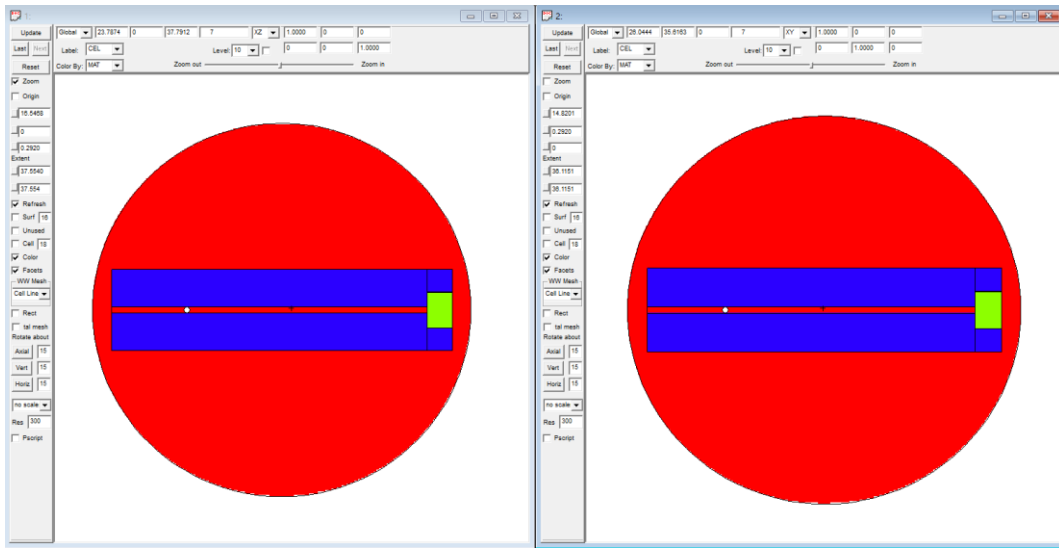
Fig. III-12. Gamma-ray detection problem (left: x-z plot, right: x-y plot).

Fig. III-13 shows the deposited energy spectrum in the NaI detector from the gamma rays emitted by the ^{60}Co source as calculated by SERPENT2, MCNP6, and GEANT4 v10.04.p02. The SERPENT2 calculation is a photon transport mode with 1 billion photon histories. The MCPLIB12 photon library and SERPENT–internal auxiliary photon data files are adopted for the SERPENT2 simulations [13]. The MCNP6 calculation is a photon–electron transport mode with 1 billion photon histories. The MCPLIB12 and e103 electron library are used for photon and electron transport, respectively [14].
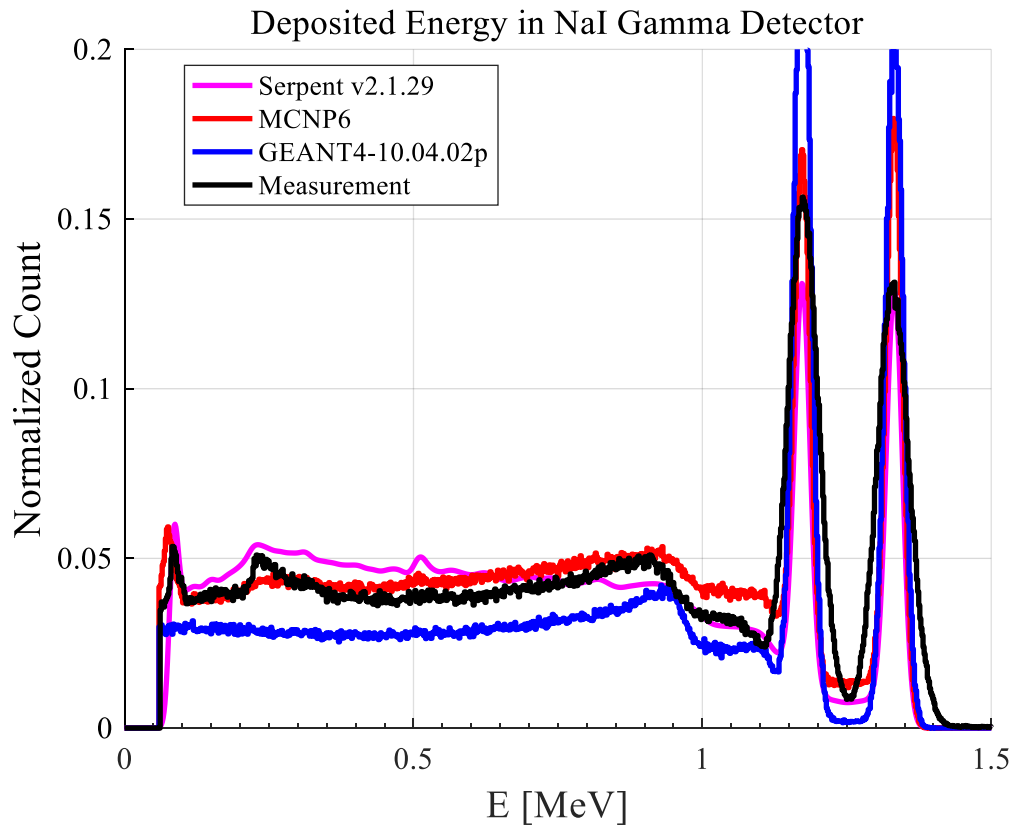
Fig. III-13. Deposited energy spectrum in the NaI detector by gamma rays from ^{60}Co source.

SERPENT2, MCNP6 and GEANT4 calculations correspond well with the measurement data in **Fig. III-13**. The 1.17 and 1.33 MeV peaks from ^{60}Co decays are visible, as well as the corresponding Compton edges at 0.96 and 1.12 MeV. Because SERPENT v2.1.29 does not have a peak energy expansion feature, the tallied counts were extended through a MATLAB post-processing script. The SERPENT2 and MCPN6 results are closer to the measurements than those of GEANT4, especially for the 75 keV x-ray fluorescence peak and the 209 keV back-scattering peak. The three reasons why the GEANT4 results are further away from the measurements than those of SERPENT2 and MCNP6 are as follows:

First, a reflective boundary condition is applied for the sphere surface in SERPENT2 and MCNP6, whereas a leakage boundary condition is applied in GEANT4. This difference explains why the back-scattering peaks below 0.5 MeV do not appear in the GEANT4 results. For the GEANT4 simulation, it is difficult to set a reflective boundary condition for the sphere surface. Second, the reflectivity of the lead was set to 0.9 in the GEANT4 simulations, which is different from the experimental configuration. Third and finally, the physics to simulate X-ray fluorescence was turned off in GEANT4 during the calculations.

III.5. Preliminary conclusions

Based on the characteristics of the SERPENT2, MCNP6 and GEANT4 codes in terms of neutron and photon physics, the SERPENT2 code is employed to determine the neutron and gamma source spectrum at the location of the diamond detector in CROCUS (global simulation), whereas GEANT4 will be used for the detailed simulation of the response of the diamond detector (local simulation). The latest version of GEANT4 is used in this study.

The reason why SERPENT2 is selected instead of MCNP6 is that SERPENT2 has the same capacity for neutron-photon coupled simulations as MCNP6, while SERPENT2 has faster calculation performance, especially concerning the depletion calculation function.

IV. Establishment of Diamond Detector Analysis System

In Chapter IV, the modeling of the neutron and prompt gamma ray contributions and that of the delayed gamma ray contribution are introduced.

IV.1. Modeling of the neutron and prompt gamma sources in CROCUS

Fig. IV-1 shows the neutron/prompt gamma/delayed gamma spectra generated by SERPENT2 at the location of the diamond detector in CROCUS.
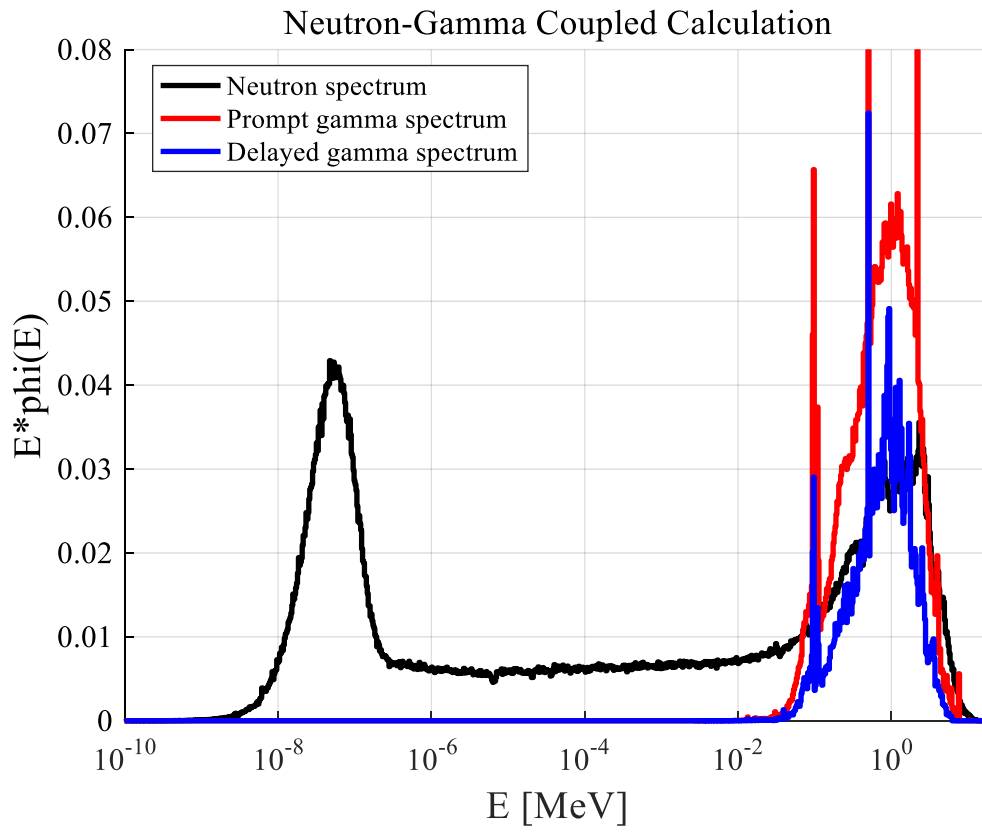
Fig. IV-1. Neutron/prompt gamma/delayed gamma spectra calculated by SERPENT2.

For the neutron and prompt gamma spectra calculation, criticality calculations in neutron–photon transport mode are carried out using the SERPENT2 full-core model of CROCUS. The ENDF/B-VII.0 neutron library with $S(\alpha,\beta)$ data at 293.6 K and the MCPLIB12 photon library are employed. 500 active cycles of 2 million histories are run and 100 inactive cycles are discarded before the start of the active cycle. The full-core simulation accounts for the production of prompt gamma photons from fission reactions, radiative captures, and inelastic scattering.

In **Fig. 7**, the neutron spectrum was normalized to have an area of 1, and the prompt gamma spectrum was normalized to have an area of the neutron-to-prompt-gamma spectrum ratio (~0.62) because the ratio between the prompt gamma and neutron fluxes tallied by SERPENT2 is 0.62. For the neutron spectrum, CROCUS shows a typical light water reactor spectrum. For the prompt and delayed gamma spectra, two or three peaks are observed: the electron-positron pair annihilations at 0.511 MeV, the radiative capture peak on hydrogen in the water at 2.223 MeV, and the radiative capture peak of aluminum in the cladding at 7.724 MeV [15-17].

For the neutron and prompt gamma spectra calculation, a two-step approach is employed. First, CROCUS full-core simulation (so-called "global" simulation) is carried out by SERPENT2 to determine the neutron and prompt gamma source at the location of the diamond detector. Subsequently, detailed results for the diamond detector problem are obtained by GEANT4 (so-called "local" simulation). For the global simulation, criticality calculations in the neutron-photon transport mode are carried out using the SERPENT2 full-core model of CROCUS. The ENDF/B-VII.0 neutron library with $S(\alpha,\beta)$ data at 293.6 K, and the MCPLIB12 photon library are employed. 500 active cycles of 2 million histories are run and 100 inactive

cycles are discarded before the start of the active cycle. The full-core simulation accounts for the production of prompt gamma photons from fission reactions, radiative captures, and inelastic scattering. The modeling method of the delayed gamma spectrum calculation is described in the next section in detail.

IV.2. Modeling of the delayed gamma sources in CROCUS

The calculation method for obtaining the delayed fission gamma spectrum at the location of the diamond detector is as follows.

First, a SERPENT2 depletion calculation of the full CROCUS core is performed. The irradiation time in the experiment (~160 min) is divided into four sub-steps of 40 min in the SERPENT2 simulation. The power of the reactor is set equal to 26 W to set an environment similar to that of the experiment. The number of fuel depletion cells is equal to 2560 (512 fuel cell × 5 plane sub-divided along z-axis). This depletion calculation makes it possible to obtain the depleted fuel compositions at 0, 40, 80, 120, and 160 min after the beginning of the irradiation. A total of 1334 nuclides are used for the SERPENT2 depletion calculation. The delayed activation gamma sources corresponding to the depleted fuel compositions are determined for each fuel pin with a STREAM-SNF gamma-source-term calculation.

The strengths of the delayed fission gamma source in the UO_2 pin and U-metal pin next to the diamond detector at 0, 40, 80, 120, and 160 min are displayed in **Fig. IV-2**. The corresponding normalized spectra are shown in **Fig. IV-3** and **Fig. IV-4**, respectively.
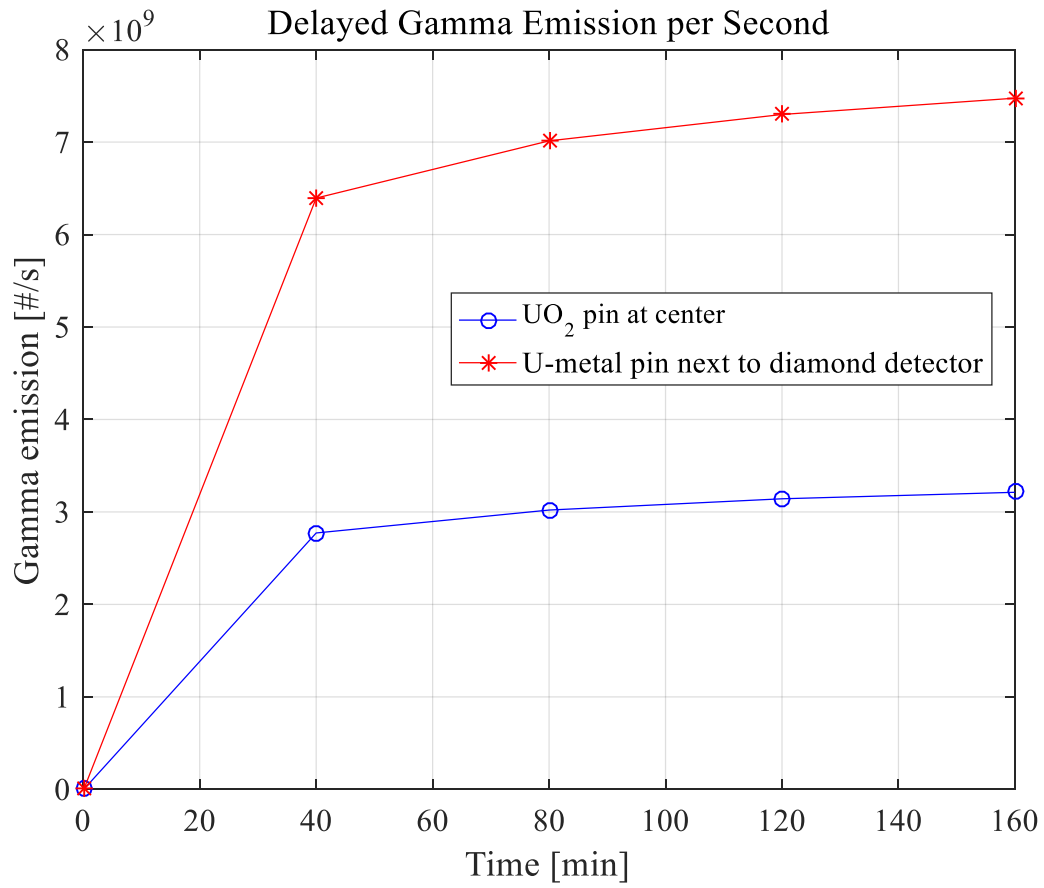
Fig. IV-2. Delayed gamma source strength as a function of the irradiation time.

The delayed gamma source is normalized along time as follows.

$$\overline{S_{i,j}} = \frac{20 \times \left\{ \left(S_{i,j,0} + S_{i,j,1} \right) + \left(S_{i,j,1} + S_{i,j,2} \right) + \left(S_{i,j,2} + S_{i,j,3} \right) + \left(S_{i,j,3} + S_{i,j,4} \right) \right\}}{160}, \qquad (4)$$

where $S_{i,j,k}$ is the source (gammas per second), for fuel pin index i, energy group index j, and time step index k, calculated by STREAM-SNF, and $\overline{S_{i,j}}$ is the average source. The numerator on the right-side term is the same as the area under the lines in **Fig. IV-2**.
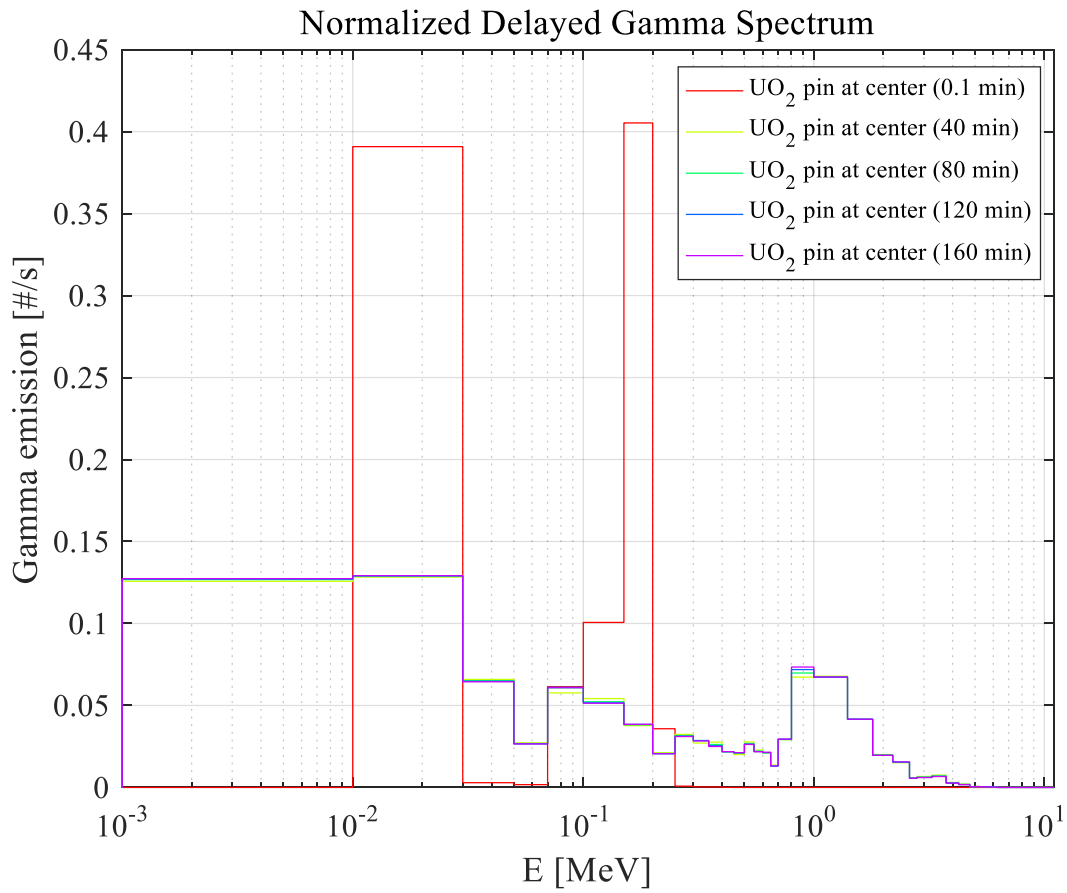
Fig. IV-3. Delayed gamma source spectrum of UO_2 pin in the center of CROCUS.
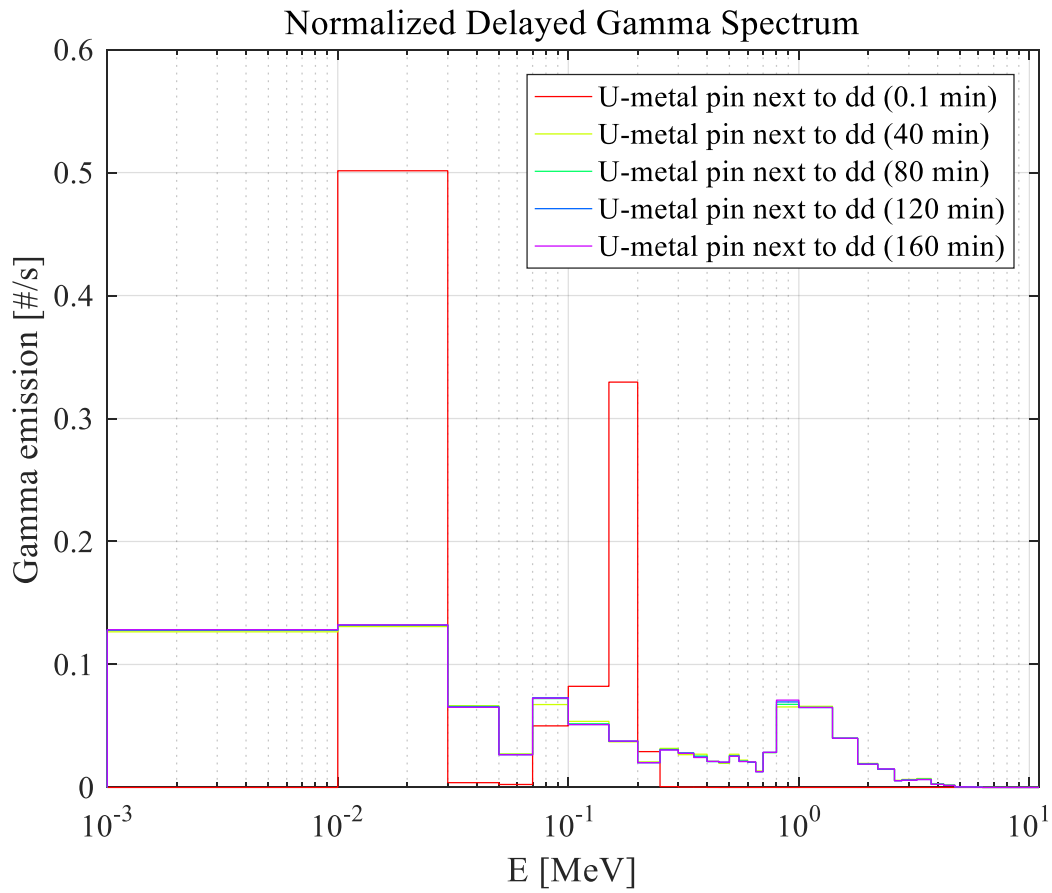
Fig. IV-4. Delayed gamma source spectrum in a U-metal pin next to the diamond detector.

As **Figs. IV-3 and IV-4** show that the spectrum differences over the irradiation time are small except for 0-burnup, the four delayed gamma sources are averaged over time, which results in one gamma source for each pin in CROCUS. The pin-wise delayed gamma source is inserted to each pin in the SERPENT2 input file. The gamma spectrum is tallied at the location of the diamond detector from the SERPENT2 photon transport calculation with the pin-wise source. By using this delayed gamma spectrum at the location of the diamond detector, GEANT4 simulation is performed to obtain detailed delayed gamma results.

IV.3. Normalization of the flux

The neutron and prompt gamma fluxes per neutron source are obtained from a SERPENT2 criticality calculation and normalized to the CROCUS reactor power during irradiation according to Eq. (5).

$$\phi \left[\frac{particle}{cm^2 \cdot s} \right] = \frac{P[W] \times \bar{v} \left[\frac{neutron}{fission} \right]}{\left(1.6022 \times 10^{-13} \frac{J}{MeV} \right) \times w_f \left[\frac{MeV}{fission} \right]} \frac{1}{k_{eff}} \phi_{tallied} \left[\frac{1}{cm^2} \right], \qquad (5)$$

where ϕ is either the neutron flux or the prompt gamma flux, the particle is either the neutron or prompt gamma, P is the power of CROCUS in W, $\bar{v}$ is the average number of neutrons emitted by a fission in CROCUS, w_f is the energy emitted by a fission in CROCUS, k_{eff} is the multiplication factor of CROCUS, and $\phi_{tallied}$ is the neutron or prompt gamma flux per neutron source as tallied by a detector function in SERPENT2 [18].

Meanwhile, the delayed gamma flux was normalized as follows.

$$\phi \left[\frac{photon}{cm^2 \cdot s} \right] = \sum_{i \in (all\ fuel\ pins)} \left(\sum_{j \in (energy\ group)} \overline{S_{i,j}} \right) \left[\frac{photon}{s} \right] \times \phi_{tallied} \left[\frac{1}{cm^2} \right], \qquad (6)$$

where $\overline{S_{i,j}}$ is the average source previously described in Eq. (4). Eq. (6) presents a different normalization scheme from Eq. (5) because the source particle in Eq. (6) is gamma, and not neutron like in Eq. (5).

Table VI-1 summarizes the calculation results of the neutron, prompt gamma, and delayed gamma transport.

Table VI-1. Calculation results in CROCUS neutron/gamma transport.

Parameter	Value
$P[\mathrm{W}]$	26
$\bar{v}\left[\dfrac{\text{neutron}}{\text{fission}}\right]$	2.43
$w_f\left[\dfrac{\text{MeV}}{\text{fission}}\right]$	193.4834
k_{eff}	1.00187 ± 0.00002
$\phi_{neutron}\left[\dfrac{\text{neutron}}{\text{cm}^2 \cdot \text{s}}\right]$	$1.61 \times 10^9 \pm 2.26 \times 10^6$
$\phi_{g,prompt}\left[\dfrac{\text{photon}}{\text{cm}^2 \cdot \text{s}}\right]$	$1.00 \times 10^9 \pm 4.11 \times 10^6$
$\displaystyle\sum_{i \in (\text{all fuel pins})} \left(\sum_{j \in (\text{energy group})} \overline{S_{i,j}} \right)\left[\dfrac{\text{photon}}{\text{s}}\right]$	6.47×10^{12}
$\phi_{g,delayed}\left[\dfrac{\text{photon}}{\text{cm}^2 \cdot \text{s}}\right]$	$4.71 \times 10^8 \pm 2.17 \times 10^6$
$\dfrac{\phi_{g,delayed}}{\phi_{g,prompt}}$	$47.2\% \pm 0.4\%$
$\dfrac{\phi_{gamma}}{\phi_{neutron}} = \dfrac{\phi_{g,prompt} + \phi_{g,delayed}}{\phi_{neutron}}$	$91.4\% \pm 0.5\%$

In **Table 1**, the w_f value was from the ENDF file (mf=1, mt=458 for ^{235}U) [19]. The delayed-to-prompt gamma fraction is 47.2%, and the gamma-to-neutron fraction is 91.4%. The delayed gamma-rays occur mainly because of the beta decay of ^{239}U atoms (~7% of the total gamma emission).

V.   Application of Diamond Detector Analysis System

Chapter V analyzes the particle interaction results further using GEANT4 v10.04.p02, especially focusing on the relationship between the deposited energy and the charge collection pulse width [20].

The gamma contributions (approximately 73% of the neutron + gamma contributions in the energy range of over 0.75 MeV as **Fig. V-1** shows) are not considered in Sections V.1 and V.2.
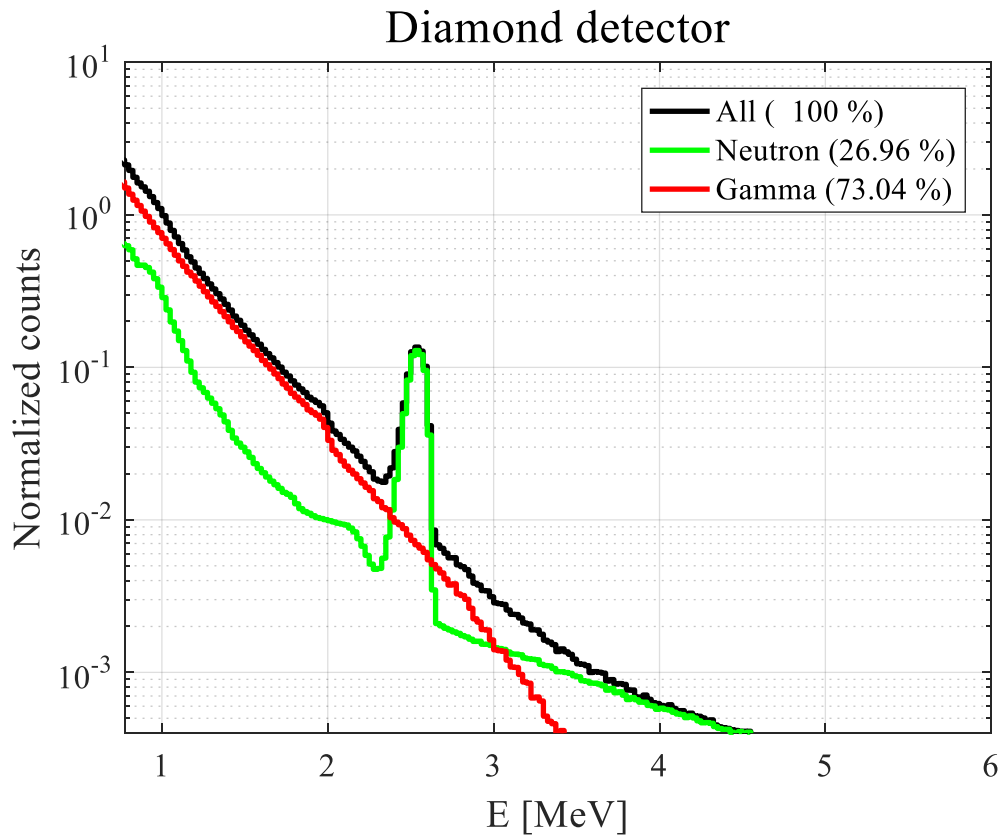
Fig. V-1. Neutron and gamma contributions for GEANT4 pulse energy spectrum.

V.1. Pulse energy spectrum

Fig. V-2 shows the deposited energies through each type of interaction with the diamond crystal. In **Fig. V-2**, "Neutron inelastic scattering" means that a neutron directly causes an inelastic scattering with a carbon atom of the diamond detector. "Neutron elastic scattering" means that a neutron directly causes an elastic scattering with a carbon atom of the diamond detector. "LiF converter" is the response in which the energy is deposited by an alpha or triton produced by the reaction between ^{6}Li particles and thermal neutrons. "Proton recoil" means that the energy is deposited in the diamond crystal by a proton ejected from the polyethylene collimator or the holder by a neutron collision. "Else" refers to other reactions by the electrons, mainly a multiple Coulomb scattering. "Neutron" refers to the sum of all cases.
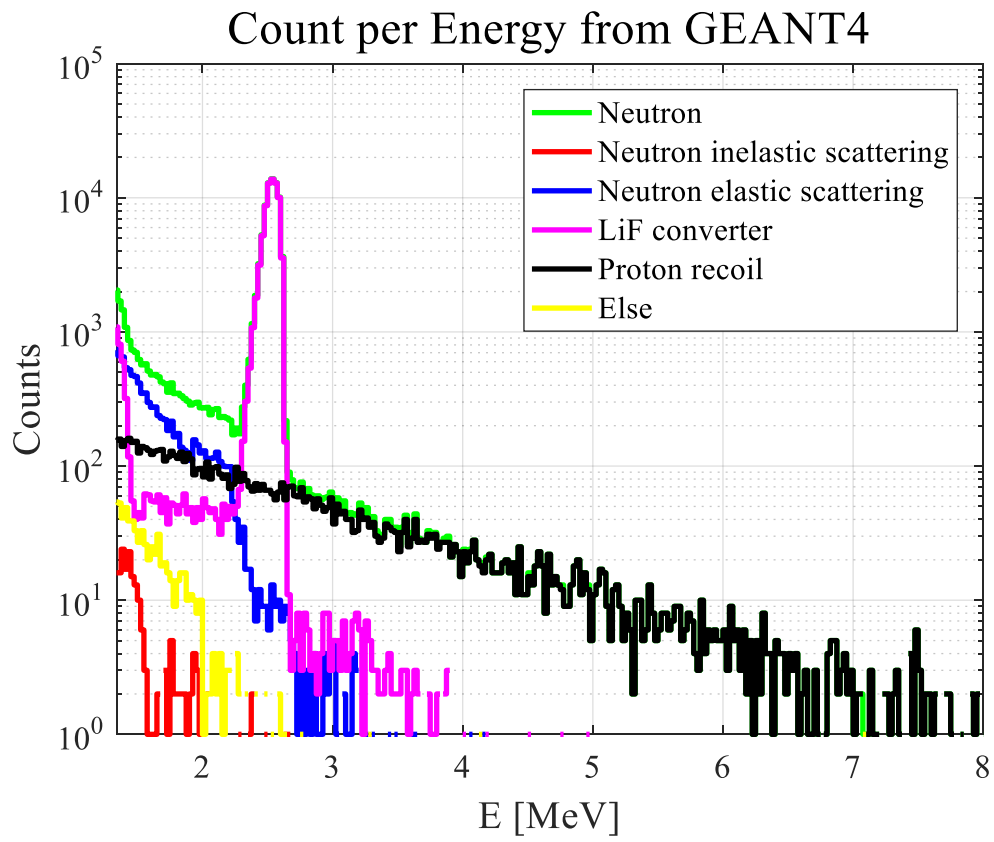
Fig. V-2. Deposited energy from GEANT4 simulation.

In the measurements, an amplitude trigger was set to 15 mV. Because the pulse caused by the thermal neutron interactions is rectangular, the threshold energy set by the voltage of 15 mV is calculated as

$$\frac{15 \text{ mV} \times 10 \text{ ns}}{112 \text{ pVs/MeV}} \cong 1.34 \text{ MeV},\tag{7}$$

using a conversion factor of 112 pVs/MeV. The conversion factor is set to match the roughly estimated tritium peak from the [241]Am source experiment to a well-known value (i.e., ~2.553 MeV) [3]. Similarly, the pulse shape caused by the gamma interactions is triangular, which gives

$$\frac{15 \text{ mV} \times 10 \text{ ns} \times 1/2}{112 \text{ pVs/MeV}} \cong 0.67 \text{ MeV},\tag{8}$$

assuming a drift time of 10 ns for the charged particles. The threshold energy for fast neutron scattering collisions at the BCR is

$$\frac{15 \text{ mV} \times 4.13 \text{ ns}}{112 \text{ pVs/MeV}} \cong 0.55 \text{ MeV},\tag{9}$$

with a drift time of 4.13 ns for the charged particles. Because **Fig. V-2** presents the neutron simulation results, a threshold energy of 1.34 MeV was used in **Fig. V-2**.

Fig. V-2 shows that the energy absorbed by the LiF converter response forms a tritium peak at 2.5 MeV. An alpha peak of 1 MeV does not appear on the graph owing to the cutoff

below the thermal neutron threshold energy (i.e., 1.34 MeV). The elastic, inelastic, and else

reactions are at low energies. Proton recoil has a tail that extends to high energy. This shows

that the high-energy rectangular pulses are produced by proton recoil. The fraction of each

interaction in **Fig. V-2** is listed in **Table V-1**.

Table V-1. Fraction of neutron interactions from the GEANT4 simulations.

Interaction	Fraction [%]
Neutron	100
Neutron inelastic scattering	0.17 ± 0.01
Neutron elastic scattering	9.34 ± 0.11
LiF converter	80.88 ± 0.80
Proton recoil	8.93 ± 0.10
Else	0.68 ± 0.03

In **Table V-1**, it is observed that the LiF converter reaction accounts for the largest percentage at 80.88%. The neutron elastic scattering is next at 9.34%. Another 8.93% of the total interactions is due to protons. "8.93% ± 0.10%" means that the amount of proton recoil belongs to the interval between 8.83% and 9.03% with 68% probability. The statistical uncertainties were derived from 1,400 parallel calculations.

Fig. V-3 shows the distance from the cathode to a position that each interaction occurs. The pink line in **Fig. V-3** shows that the LiF reaction can be seen mostly in the vicinity of the cathode. This is because tritium or alpha particles produced by the ^{6}Li(n,^{3}H)^{4}He reaction react quickly to the diamond sensor and lose energy. The black line in **Fig. V-3** shows that the protons do not have sufficient energy to cross the diamond crystal. They release their full energies near the electrodes with the same probability of interacting at the anode and cathode. The other responses are distributed evenly over distance.
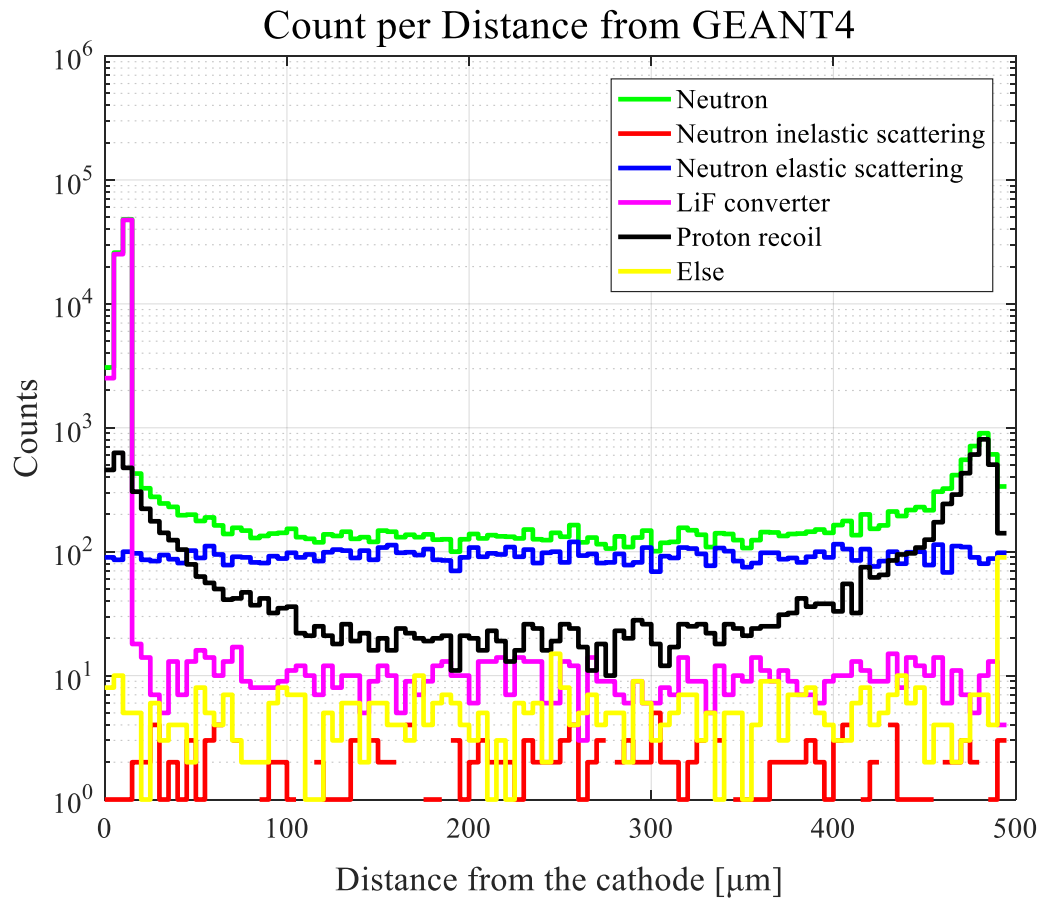
Fig. V-3. Distance from the cathode through GEANT4 simulation.

V.2. Scatter plot

A scatter plot in this study is a single view of the absorbed energy spectrum for each width. Here, the width is set at a constant position relative to the maximum amplitude of each pulse. For example, the width in **Fig. I-1** was set at 12.5% of the maximum amplitude. Scatter plots are interesting because they provide pulse width and energy at the same time; however, they are limited in detailed analysis for experimental results. This raises the need for simulations.

To draw a scatter plot using the simulation results, the width and energy of the pulses should be determined first. The energy and position in **Figs. V-2** and **V-3** are directly provided by GEANT4. The pulses are produced from them as follows:

(1) Through the GEANT4 simulations, the deposited energy and location of each reaction are extracted and summarized.

(2) With a bias voltage of 400 V, the electron drift velocity is around 50 μm/ns and the hole velocity around 70 μm/ns. A voltage of 400 V was applied in the measurements of this study.

(3) The drift times are calculated by dividing the distance from the electrodes by the velocity of the charged particles in step (2).

(4) The energies are converted to areas in pVs (voltage in mV multiplied by time in ns) by multiplying with the conversion factor 112 pVs/MeV.

(5) The areas are divided equally because the energies produced by an electron and a hole are similar.

(6) The areas of the electron and hole are divided by the drift times in step (3). The voltages are then obtained.

(7) The voltages of the electron and hole are summed up.

(8) If an ionization reaction occurs near the electrodes, the drift time will be very small, and the voltage will become too high.

(9) In actual measurements, because the high voltage is not recorded in the pulse signal, the pulse is recorded as rectangular regarding the reactions occurring at the vicinity of the electrodes. This means that the high voltage is considered zero.

(10)   The voltage obtained in step (7) or (9) is used to determine if it exceeds the threshold voltage of 15 mV.

(11)   If exceeded, the greater of the two drift times is considered a charge collection pulse width. This charged collection pulse width (at 0% of the maximum by energy obtained in this manner) is defined as a calculation width.

Fig. V-4 shows an example of pulse shapes for each interaction generated from GEANT4.
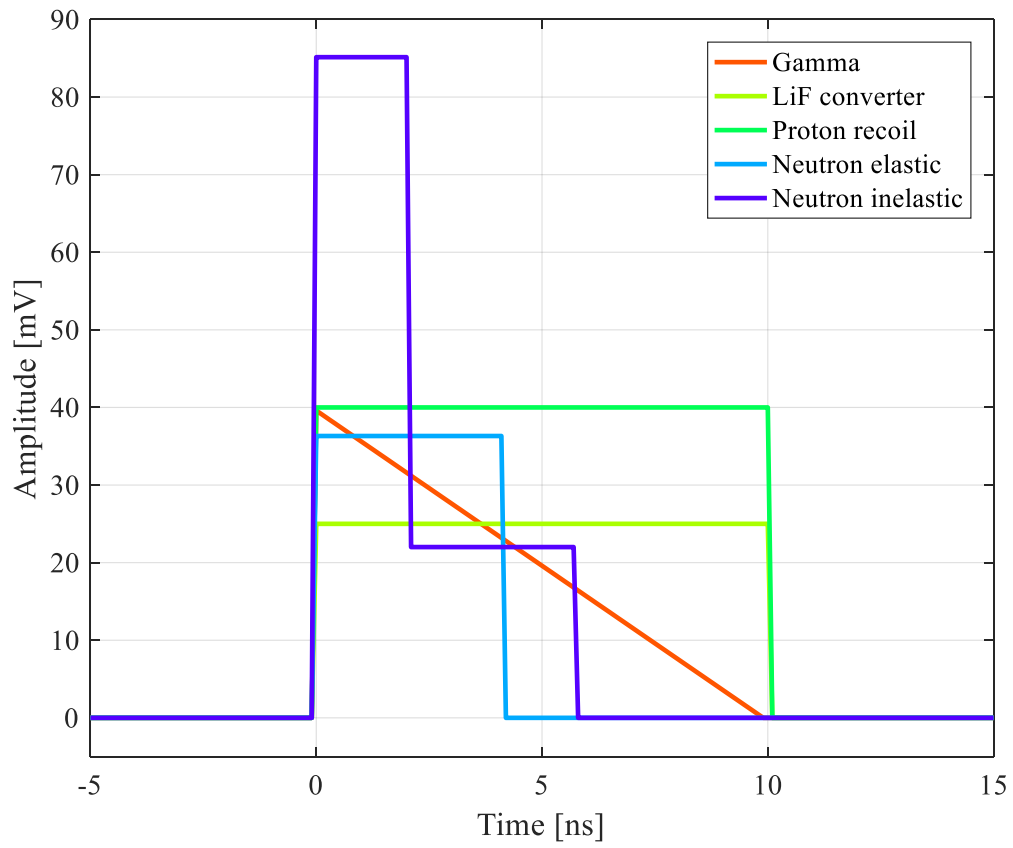
Fig. V-4. Example of pulse shapes for each interaction generated from GEANT4.

In **Fig. V-4**, the pulse from the gamma interaction is triangular, that from inelastic scattering collision is a step-shape, and pulses from the LiF converter, proton recoil, and elastic scattering collision are rectangular. The energy of the pulse from the LiF converter response is 2.5 MeV that is the tritium peak. The energy of the pulse from the proton recoil reaction is 4 MeV, showing consistency with the results in **Fig. V-2**. It is observed that neutron inelastic scattering occurred 100 μm away from the anode, whereas neutron elastic scattering occurred at the BCR.

Fig. V-5 shows a scatter plot between the deposited energy and the calculation width generated by GEANT4. The energy and calculation width were calculated by the above procedures.
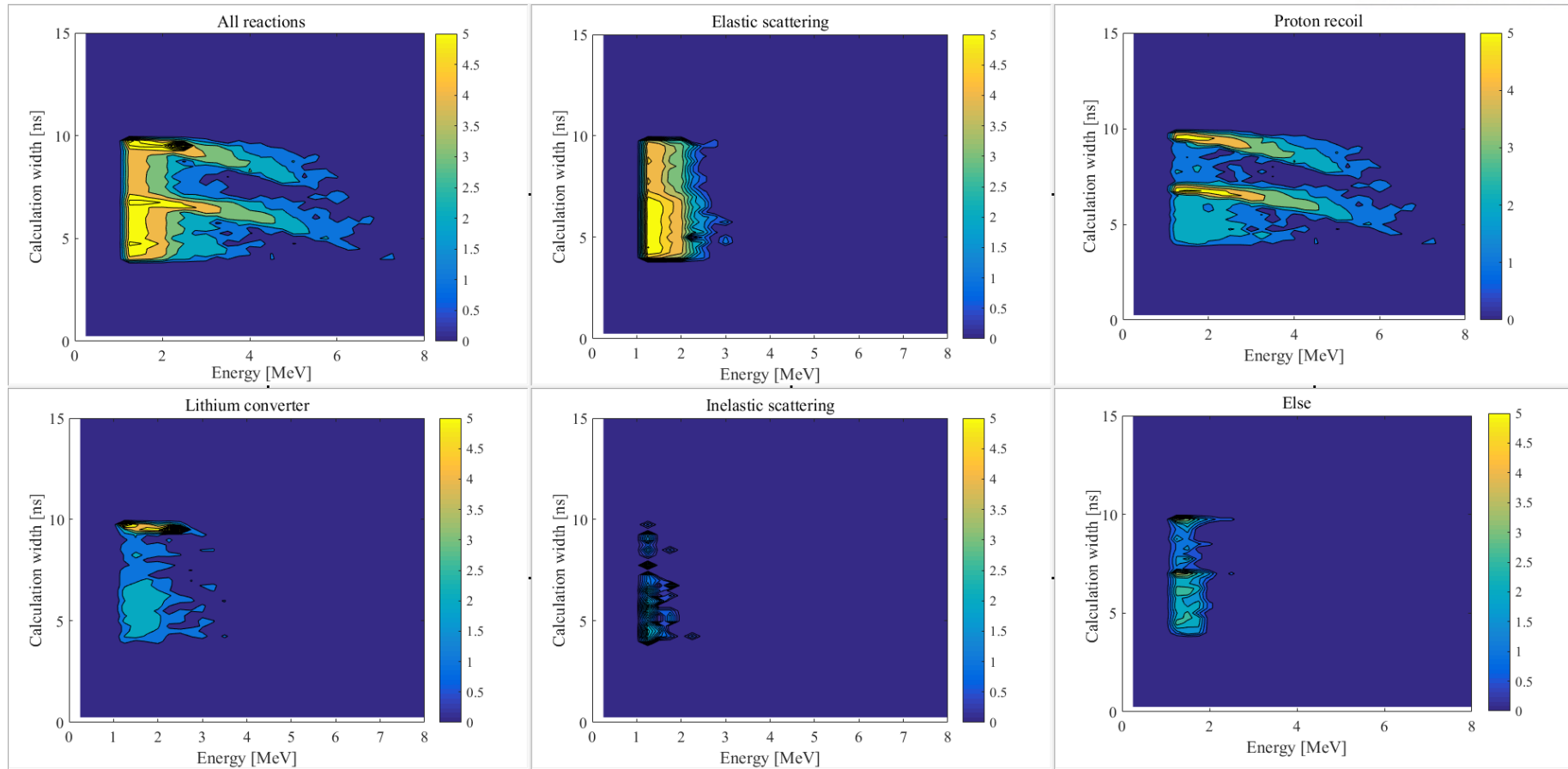
Fig. V-5. Scatter plot (deposited energy vs. calculation width) from GEANT4.

In **Fig. V-5**, only energy deposition greater than 1.34 MeV is counted. For the elastic scattering reactions, because the responses occur overall inside the diamond sensor, the calculation width is evenly distributed between 4 and 10 ns. As mentioned, with the voltage of 400 V, the electron drift velocity is approximately 50 μm/ns, and the hole velocity is approximately 70 μm/ns. While both the hole and electron drift velocities contribute to the signals observed between 4 and 7 ns, only the electron drift contributes to the calculation width between 7 and 10 ns.

In the case of the proton recoil response, two bands appear, one by protons impacting the anode and the other by protons impacting the cathode. Protons entering the cathode produce electrons and holes, of which only electrons contribute to the generation of pulses because the hole drift time is too short to be captured. Protons entering the anode also produce both electrons and holes, of which only holes contribute to the generation of pulses. Owing to the velocity difference between the electrons and holes, bands are formed at different widths, one at 7 ns and the other at 10 ns.

When a neutron reacts to the LiF converter, a pair of an alpha and a triton is created, one of which is then reactive at the cathode when it enters the diamond sensor. Because the alpha and triton always reacts only on the cathode side, only electron drifts contribute to the generation of the pulses of 10 ns at all times.

In "All reactions" of **Fig. V-5**, a small ridge around 5 ns is observed. This ridge appears because of the pulses resulting from energy deposition near the BCR, because a large amount of elastic scattering is recorded around the BCR owing to the larger amplitude for the same energy deposition, even though the probability of the elastic scattering is homogeneous in the

crystal as shown in **Fig. V-3**.

VI.   Assessment of Model Performance against Experimental Data

Fig. VI-1 shows the energy spectra from the GEANT4 calculations using the MCNP6-generated neutron, prompt gamma, and delayed gamma spectra in **Fig. IV-1**. The energy for the measurements in **Fig. VI-1** was obtained by converting an area using a conversion factor of 112 pVs/MeV. **Fig. VI-1** shows only the results that exceed the gamma threshold energy (0.67 MeV) for both the simulation and experiment.

In **Fig. VI-1**, the green and red lines indicate energy deposited by neutron and gamma interactions from the GEANT4 simulation, respectively, the black line is the total deposited energy as the sum of the green and red lines, and the blue line indicates the measured data combining the effects of the neutrons and gamma rays. These lines were normalized so that the blue and black lines overlapped at the threshold energy of 1.34 MeV. Both the green and blue lines show the triton peak at 2.553 MeV, which is caused by a thermal neutron interaction with ^{6}Li particles.

The GEANT4 results show that 27% of the total responses are neutron effects and 73% are gamma–ray effects. The slope of the curves between 1 MeV and 2 MeV are mainly produced by gamma interactions. The high energy tail is produced by neutron interactions, especially, the proton recoil. The brown line shows the measured rectangular pulses, and the pink line shows the ^{6}Li converter responses from the GEANT4 simulation. The ^{6}Li reactions account for 14.31% and 15.13% beyond 1.34 MeV for the measurements and simulations, respectively.
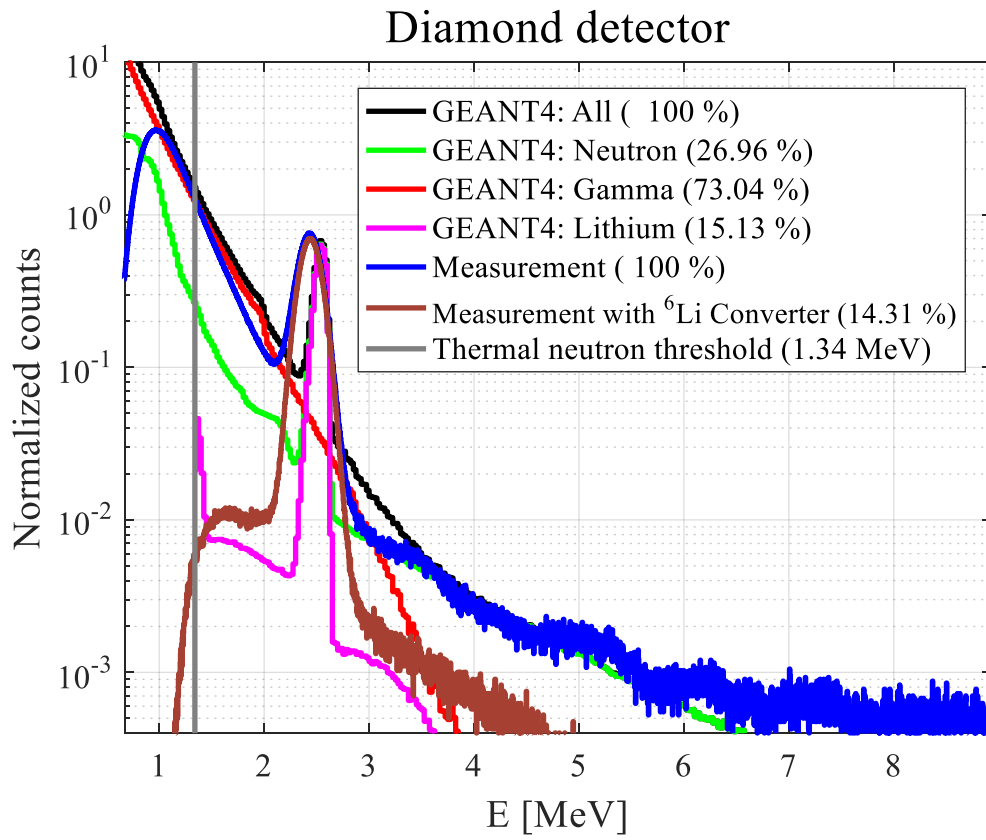
Diamond detector

Fig. VI-1. Pulse energy spectrum comparison with the measured data.

VII. Conclusions and Perspectives

The measurement data acquired from a diamond detector in a mixed neutron-photon field of the CROCUS zero-power reactor was analyzed and compared with detailed Monte Carlo calculations in this study. Three contributions to the diamond detector response (neutron, prompt gamma, and delayed gamma) were calculated. The contributions of the prompt gamma rays and neutrons were investigated by a SERPENT2/GEANT4 two-step procedure. SERPENT2 full-core criticality calculations were first performed to obtain the neutron and prompt gamma spectra at the location of the diamond detector in CROCUS, and then GEANT4 v.10.04.p02 fixed-source calculations were performed to simulate the transport of charged particles in the diamond detector alone using the previous neutron and prompt gamma spectrum as the source. The contribution of delayed fission gamma was investigated by a SERPENT2/STREAM-SNF/GEANT4 three-step procedure: a SERPENT2 full-core depletion calculation was first performed to obtain depleted fuel compositions during irradiation, then the corresponding delayed gamma source was calculated from the depleted fuel compositions by the STREAM-SNF source-term calculation, and finally, the delayed gamma spectrum was used as the source in a GEANT4 v10.04.p02 fixed-source simulation of the diamond detector alone.

Through the presented calculation scheme, the calculated fraction of the prompt gamma flux over the neutron flux at the location of the detector was ~62%, and the fraction of delayed-to-prompt gamma fluxes was ~47.2% for a 160-min irradiation at 26 W power. Using the spectra at the location of the diamond detector as the fixed source, the local GEANT4 simulations of the diamond detector alone showed that the contributions of neutrons and gamma rays to the detector response amounted to approximately 27% and 73%, respectively.

With an LiF converter, both calculation and experimental results showed an approximately 15% consistency of the total reactions.

Using the energies and positions of the particles contributing to the tallies in the GEANT4 simulation, numerical pulses of the diamond detector were rebuilt and used to determine a calculation width at 0% of the maximum amplitude. A scatter plot was derived accordingly and the analysis of the scatter plot revealed two bands caused by the proton recoil: one band from protons impacting the anode and the other from protons impacting the cathode. The effect of these proton recoils was also shown as a high-energy tail in a pulse energy spectrum.

Meanwhile, neutron scattering (both elastic and inelastic) collisions were distributed evenly over the distance from the electrodes in the diamond crystal. Hence, the structure observed with a higher count rate at the BCR is probably related to the amplitude of the BCR pulses being higher, and thereby it is possible to see the pulses resulting from energy deposition at the BCR better.

References

[1] Hursin, M. et al. Testing of a sCVD diamond detection system in the CROCUS reactor. *Eur. Phys. J. A* **54**, 82-92 (2018).

[2] Weiss, C., Frais-Kölbl, H., Griesmayer, E., & Kavrigin, P. Ionization signals from diamond detectors in fast-neutron fields. *Eur. Phys. J. A* **52**, 269-275 (2016).

[3] Kavrigin, P., Finocchiaro, P., Griesmayer, E., Jericha, E., Pappalardo, A., & Weiss, C. Pulse-shape analysis for gamma background rejection in thermal neutron radiation using CVD diamond detectors. *Nucl. Instrum. Meth. A* **796**, 88-91 (2015).

[4] Leppänen, J. et al. The Serpent Monte Carlo code: Status, development and applications in 2013, *Ann. Nucl. Energy* **82**, 142-150 (2015).

[5] Agostinelli, S. et al. GEANT4 – a simulation toolkit. *Nucl. Instrum. Meth. A* **506**, 250-303 (2003).

[6] Ebiwonjumi, B., Choi, S., Lemaire, M., Lee, D., Shin, H. C., & Lee, H. S. Verification and validation of radiation source term capabilities in STREAM. *Ann. Nucl. Energy* **124**, 80-87 (2019).

[7] Ebiwonjumi, B., Choi, S., Lemaire, M., Lee, D., & Shin, H. C. Validation of lattice physics code STREAM for predicting pressurized water reactor spent nuclear fuel isotopic inventory. *Ann. Nucl. Energy* **120**, 431-449 (2018).

[8] Kim, W., Hursin, M., Pautz, A., Vincent, L., Pavel, F. & Lee, D. Determination of the activity inventory and associated uncertainty quantification for the CROCUS zero power research reactor. *Ann. Nucl. Energy* **136**, 107034 (2020).

[9] Pelowitz, D. B. (Ed.), et al. MCNP6 User's Manual, Version 1.0, Technical Report LA-CP-13-00634, Los Alamos National Laboratory, NM, USA (2013).

[10] Zboril, M. et al. Simulation of the neutron response functions of diamond detectors with

the NRESP code. 1st EPS Conference on Plasma Diagnostics, 14-17 April, 2015, Villa Mondragone, Frascati (Rome), Italy.

[11] Garcia, A. R. et al. New physics model in GEANT4 for the simulation of neutron interactions with organic scintillation detectors. *Nucl. Instrum. Meth. A* **868**, 73-81 (2017).

[12] Dietze, G. & Kelin, H. NRESP4 and NEFF4: Monte Carlo codes for the calculation of neutron response functions and detection efficiencies for NE213 scintillation detectors. Technical Report PTB-ND-22, Physikalisch-Technishe Bundesanstalt, Braunschweig, Germany (1982).

[13] Kaltiaisenaho, T. Implementing a photon physics model in Serpent 2. Mater's thesis, Aalto University, Finland (2016).

[14] Hughes, H. G. Recent Developments in Low-Energy Electron/Photon Transport for MCNP6. Technical Report LA-UR-12-23333, Los Alamos National Laboratory, NM, USA (2012).

[15] Panzarasa, G., et al. Positron annihilation spectroscopy: a new frontier for understanding nanoparticle-loaded polymer brushes. *Nanotechnology* **27**, 02LT03-08 (2016).

[16] Sibczynski, P., et al. Monte Carlo N-Particle simulations of an underwater chemical threats detection system using neutron activation analysis. *J. Instrum.* **14**, P09001-P09008 (2019).

[17] Schrack, R. A., & Bowman, C. D. (Ed.). Nuclear Cross Sections and Technology Volume II, Proceedings of a Conference, Washington, D.C., March 3-7, National Bureau of Standards Special Publication 425 (1975).

[18] Snoj, S., & Ravnik, M. Calculation of Power Density with MCNP in TRIGA Reactor. International Conference Nuclear Energy for New Europe 2006, Portoroz, Slovenia (2006).

[19] Chadwick, M. B., et al. ENDF/B-VII.0: Next Generation Evaluated Nuclear Data Library for Nuclear Science and Technology. Technical Report UCRL-JRNL-225066, Lawrence Livermore National Laboratory, CA, USA (2006).

[20] Kong, C., Lee, D., & Hursin, M. Transactions of Korean Nuclear Society, 25-26 October, 2018, Yeosu, Republic of Korea.

Acknowledgment

마지막으로 비천한 저를 여기까지 인도하신 하나님, 고맙습니다. 사랑합니다.

Curriculum Vitae

Chidong Kong

Tel.: +82-10-7748-9426 / E-mail: kcd1006@gmail.com

AFFILIATION

Ph.D. Candidate

Computational Reactor Physics and Experiment Laboratory (CORE)

Department of Nuclear Engineering

Ulsan National Institute of Science and Technology (UNIST)

50 UNIST-gil, Ulsan 44919, Republic of Korea

EDUCATION

- **Doctor of Engineering**
  - UNIST CORE (2013.09 ~ 2020.02, 6.5 years)
  - Major: Nuclear reactor physics
  - Advisor: Prof. Deokjung Lee
  - Ph.D. Thesis: Establishment and Application of Diamond Detector Analysis System
- **Bachelor of Engineering**
  - UNIST (2010.03 ~ 2013.08, 3.5 years)
  - Major: Nuclear engineering

WORK EXPERIENCE

- **UNIST CORE, Ph.D. Candidate (2013.09 ~ 2020.02)**
  - Best Estimate Plus Uncertainty (BEPU) for whole-core transient problem
  - Detector response modeling and nuclear instrumentation simulation
  - Numerical simulation and experiment of subcriticality estimation

- **EPFL, Switzerland (2018.06 ~ 2018.08)**
  - Numerical analysis on sCVD diamond detector in CROCUS

- **OECD/NEA, France (2016.08 ~ 2017.01)**
  - Literature survey and review of back-end fuel cycle policies in the world

RESEARCH INTEREST

- Multi-physics uncertainty quantification and BEPU
- Simulation and investigation of particle interactions in detectors
- Nuclear reactor subcriticality measurement

CERTIFICATE

- **Award and Scholarship**
  - KNS NET impact factor – Bronze prize, Korean Nuclear Society (October 2015)
  - KNS excellent poster prize, Korean Nuclear Society (October 2015)

- **Membership**
  • Korean Nuclear Society

- **Training (International)**
  • KUCA research reactor experiment (Osaka, Japan, 2017)
  • MeV summer school (Idaho, USA, 2014)
  • Nuclear fuel cycle education (Tohoku, Japan, 2014)
  • KUCA research reactor experiment (Osaka, Japan, 2013)
  • Korea-Japan joint summer school (Osaka, Japan, 2012)

- **Training (Domestic)**
  • Visual MCNP6 editor workshop (Daejeon, 2015)
  • Long-life in-core instrumentation workshop (Daecheon, 2015)
  • Nuclear design education, KAERI (Daejeon, 2015)
  • Spent fuel criticality analysis education, KHNP CRI (Daejeon, 2015)
  • Simulator education, KAERI (Daejeon, 2015)
  • McCARD developer training course (Seoul, 2015)
  • Monte Carlo theory and MCNP user training (Seoul, 2014)
  • MCNP6 workshop, KAERI NTC (Daejeon, 2014)
  • Nuclear design education, KHNP CRI (Daejeon, 2014)
  • McCARD user training course (Seoul, 2013)
  • Practical shell programming for system administrator, Samsung SDS (Seoul, 2013)
  • Signal processing with MATLAB, MathWorks Training Services (Seoul, 2013)
  • Whole core transport analysis seminar, KAERI (Muju, 2013)

ENGLISH CERTIFICATION

TOEIC 810

PUBLICATION

- **SCI journal (9 papers published; 1 paper being prepared)**
  1. **Chidong Kong**, Matthieu Lemaire, Bamidele Ebiwonjumi, Deokjung Lee, Pavel Kavrigin, Christina Weiss, Erich Griesmayer, Mathieu Hursin[*], "Physical interaction analysis in a mixed neutron and photon field of diamond detector", Nat. Commun., being prepared.
  2. **Chidong Kong**, Ho Cheol Shin, Deokjung Lee[*], "Sensitivity analysis source intensity and time bin size for the Rossi-alpha method in a numerical reactor model", Ann. Nucl. Energy **130**, pp. 157-163 (2019).
  3. **Chidong Kong**, Jiwon Choe, Seongpil Yum, Jaerim Jang, Woonghee Lee, Hanjoo Kim, Wonkyeong Kim, Nguyen Hoang Nhat Khang, Nguyen Dong Cao Tung, Vutheam Dos, Deokjung Lee[*], Ho Cheol Shin, Masao Yamanaka, Cheol Ho Pyeon, "Application of advanced Rossi-alpha technique to reactivity measurements at Kyoto University Critical Assembly", Ann. Nucl. Energy **118**, pp. 92-98 (2018).

4. **Chidong Kong**, Ho Cheol Shin, Deokjung Lee[*], "Lifetime Extension of In-Core Self-Powered Neutron Detector Using New Emitter Materials", Int. J. Energ. Res. **41**, pp. 2405-2412 (2017).

5. **Chidong Kong**, Hyunsuk Lee, Taewoo Tak, Si Hwan Kim, Seokjean Lyou, Deokjung Lee[*], "Accuracy Improvement of Boron Meter Adopting New Fitting Function and Multi-detector", Nucl. Eng. Technol. **48**, pp. 1360-1367 (2016).

6. **Chidong Kong**, Eunki Lee, Deokjung Lee[*], "Stability improvement of noise analysis method in the case of random noise contamination for subcriticality measurements", Ann. Nucl. Energy **71**, pp. 245-253 (2014).

7. Peng Zhang, Hyunsuk Lee, **Chidong Kong**, Jiwon Choe, Jiankai Yu, Farrokh Khoshahval, Deokjung Lee[*], "Practical Monte Carlo simulation using modified power method with preconditioning", Ann. Nucl. Energy **127**, pp. 372-384 (2019).

8. Matthieu Lemaire, Hyunsuk Lee, Bamidele Ebiwonjumi, **Chidong Kong**, Wonkyeong Kim, Yunki Jo, Jinsu Park, Deokjung Lee[*], "Verification of photon transport capability of UNIST Monte Carlo code MCS", Comput. Phys. Commun. **231**, pp. 1-18 (2018).

9. Yunki Jo, **Chidong Kong**, Jiankai Yu, Sihwan Kim, Deokjung Lee[*], "High accuracy boronometer design developed for light water reactors", Ann. Nucl. Energy **110**, pp. 25-30 (2017).

10. Sooyoung Choi, **Chidong Kong**, Deokjung Lee[*], Mark Williams, "A New Equivalence Theory Method for Treating Doubly Heterogeneous Fuel – II: Verifications", Nucl. Sci. Eng. **180**, pp. 41-57 (2015).

- **International and Domestic Conference (39 papers)**

1. **Chidong Kong**, Deokjung Lee[*], Mathieu Hursin, "Simulation of a Diamond Detector installed in the CROCUS Reactor", KNS Autumn Meeting, Yeosu, Korea, October 24-26 (2018).

2. **Chidong Kong**, Chang Keun Jo, Deokjung Lee[*], "Implementation of Iterative Resonance Integral Table and Subgroup Methods in STREAM for High Temperature Reactor Analysis", KNS Spring Meeting, Jeju, Korea, May 16-18 (2018).

3. **Chidong Kong**, Hyunsuk Lee, Matthieu Lemaire, Wonkyeong Kim, Yunki Jo, Jinsu Park, Jiwon Choe, Bamidele Ebiwonjumi, Deokjung Lee[*], "Introduction to UNIST Spent Nuclear Fuel Transportation Package Analysis Code System", RPHA17, Chengdu, China, August 24-25 (2017).

4. **Chidong Kong**, Hyunsuk Lee, Si Hwan, Kim, Seokjean Lyou, Deokjung Lee[*], "Development of High Accuracy Boron Meter", International Conference on Advanced Technology Innovation 2016 (ICATI 2016), Bali, Indonesia, June 30 – July 3 (2016).

5. **Chidong Kong**, Hyunsuk Lee, Ho Cheol Shin, Kyoon-Ho Cha, Deokjung Lee[*], "Feasibility Study of Silver as Emitter of In-core Neutron Detector", KNS Spring Meeting, Jeju, Korea, May 11-13 (2016).

6. **Chidong Kong**, Hyunsuk Lee, Si Hwan Kim, Seokjean Lyou, Deokjung Lee[*], "Optimization of Boron Meter Model", ICAPP2016, Sun Valley, ID, USA, April 17-20 (2016).

7. **Chidong Kong**, Hyunsuk Lee, Si Hwan Kim, Seokjean Lyou, Deokjung Lee[*], "Sensitivity Evaluation of Boron Meter Model", KNS Autumn Meeting, Gyeongju, Korea, October 29-30 (2015).

8. **Chidong Kong**, Hyunsuk Lee, Si Hwan Kim, Seokjean Lyou, Deokjung Lee[*], "Application of Rational Function for Accuracy Improvement of Boron Meter Model", RPHA15, Jeju, Korea, September 16-18 (2015).

9. **Chidong Kong**, Jiwon Choe, Ho Cheol Shin, Deokjung Lee[*], "Impact of Isotope Separation on Burnable Absorber Performance", ANS Annual Meeting, San Antonio, TX, USA, June 7-11 (2015).

10. **Chidong Kong**, Jiwon Choe, Deokjung Lee[*], Ho Cheol Shin, "Isotope Separation Effect of Burnable Absorber for Long-cycle Boron-free Reactor Core", KNS Spring Meeting, Jeju, Korea, May 6-8 (2015).

11. **Chidong Kong**, Sooyoung Choi, Minyong Park, Deokjung Lee[*], "Application of Nuclear Power Plant Simulator for High School Student Training", KNS Autumn Meeting, Pyeongchang, Korea, October 30-31 (2014).

12. **Chidong Kong**, Sooyoung Choi, Deokjung Lee[*], "Deterministic Lattice Code Development at UNIST", PHYSOR2014, Kyoto, Japan, September 28-October 3 (2014).

13. **Chidong Kong**, Sooyoung Choi, Deokjung Lee, "Method of Characteristics Code Development at UNIST", ANS Annual Meeting, Reno, NV, USA, June 15-19 (2014).

14. **Chidong Kong**, Deokjung Lee[*], "STREAM Solutions for the Two-Dimensional C5G7 MOX Benchmark Problem", KNS Spring Meeting, Jeju, Korea, May 28-30 (2014).

15. **Chidong Kong**, Deokjung Lee[*], "TICTOC Solutions for the Two-Dimensional C5G7 MOX Benchmark Problem", PHYTRA3, Tetouan, Morocco, May 11-14 (2014).

16. **Chidong Kong**, Eunki Lee, Deokjung Lee[*], "Incorporation of Random Noise into Rossi-alpha Technique", ANS Winter Meeting, Washington D.C., USA, November 10-15 (2013).

17. **Chidong Kong**, Eunki Lee, Deokjung Lee[*], "Performance Evaluation of Power Spectral Density Method for Subcriticality Monitoring of Model Reactor Problem", KNS Spring Meeting, Gwangju, Korea, May 30-31 (2013).

18. **Chidong Kong**, Eunki Lee, Deokjung Lee[*], "Feasibility Study of Noise Analysis Methods on Virtual Thermal Reactor Subcriticality Monitoring", M&C2013, Sun Valley, ID, USA, May 5-9 (2013).

19. **Chidong Kong**, Eunki Lee, Deokjung Lee[*], "Feasibility Study on Continuous Monitoring of Subcriticality by Noise Analysis Methods", ICAPP2013, Jeju, Korea, April 14-18 (2013).

20. **Chidong Kong**, Eunki Lee, Deokjung Lee[*], "Feasibility Study of Recriticality Monitoring by Noise Analysis Method", KNS Spring Meeting, Jeju, Korea, May 17-18 (2012).

21. Yunki Jo, Woonghee Lee, **Chidong Kong**, Deokjung Lee[*], "Uncertainty Analysis of UAM-LWR Benchmark with MCS", ANS Winter Meeting, Washington D.C., USA, November 17-21 (2019).

22. Siarhei Dzianisau, Hanjoo Kim, **Chidong Kong**, Dongmin Yun, Deokjung Lee[*], "Development of Barcode Model for Prediction of PWR Core Design Parameters Using Convolutional Neural Network", KNS Autumn Meeting, KINTEX, Gyeonggi, Korea, October 23-25 (2019).

23. Yunki Jo, **Chidong Kong**, Alexey Cherezov, Deokjung Lee[*], "Sensitivity and Uncertainty Analysis Capability in MCS for UAM Benchmark", M&C 2019, OR, USA, August 25-29 (2019).

24. Sungho Moon, Ser Gi Hong[*], **Chidong Kong**, Deokjung Lee, "A Computational Simulation of Sub-Criticality Measurement Using MCNP6 in Zero-power Reactor AGN-201K", KNS Autumn Meeting, Yeosu, Korea, October 24-26 (2018).

25. Mai Nguyen Trong Nhan, **Chidong Kong**, Hyunsuk Lee, Sooyoung Choi, Deokjung Lee[*], "Application of MCS Code for Spent Fuel Case Analysis", KNS Autumn Meeting, Yeosu, Korea, October 24-26 (2018).

26. Junkyung Jang, **Chidong Kong**, Seunggu Kang, Ho Cheol Shin, Hyun Chul Lee[*], "Sensitivity Analysis of SPNDs by Neutron Spectrum Using Monte Carlo Method", KNS Spring Meeting, Jeju, Korea, May 16-18 (2018).

27. Matthieu Lemaire, Hyunsuk Lee, Bamidele Ebiwonjumi, **Chidong Kong**, Wonkyeong Kim, Yunki Jo, Jinsu Park, Deokjung Lee[*], "Development of Photon-Transport Capability in UNIST Monte Carlo Code MCS", PHYSOR 2018, Cancun, Mexico, April 22-26 (2018).

28. Matthieu Lemaire, Hyunsuk Lee, Bamidele Ebiwonjumi, **Chidong Kong**, Wonkyeong Kim, Yunki Jo, Jinsu Park, Deokjung Lee[*], "Recent Work on Photon Transport with UNIST Monte Carlo Code MCS", RPHA17, Chengdu, China, August 24-25 (2017).

29. Sooyoung Choi, Minyong Park, Youzi Zheng, **Chidong Kong**, Jiwon Choe, Hanjoo Kim, Kiho Kim, Ho Cheol Shin, Deokjung Lee[*], "Development Status of Reactor Physics Code Suite in UNIST", Croatian Nuclear Society, Zadar, Croatia, June 5-8 (2016).

30. Jiwon Choe, **Chidong Kong**, Sooyoung Choi, Minyong Park, Deokjung Lee[*], Ho Cheol Shin, "Preliminary Analysis of New Secondary Shutdown System of Small Modular Pressurized Water Reactor", RPHA15, Jeju, Korea, September 16-18 (2015).

31. Ho Cheol Shin, Jiwon Choe, **Chidong Kong**, Deokjung Lee[*], "New Burnable Absorber Design with [157]Gd and [167]Er for PWRs", ICAPP2015, Nice, France, May 3-6 (2015).

32. Minyong Park, **Chidong Kong**, Sooyoung Choi, Deokjung Lee[*], Ho Cheol Shin, "Application of Macro-Micro Simulator for High School Student Training", Conference on Nuclear Training and Education 2015, Jacksonville, FL, USA, February 1-4 (2015).

33. Sooyoung Choi, **Chidong Kong**, Azamat Khassenov, Deokjung Lee[*], "Methodology and Verification of Neutron Transport Code STREAM for Analysis of Innovative Reactor Core Design", International Symposium on NPP Technology and HRD, Busan, Korea, November (2014).

34. Jiwon Choe, **Chidong Kong**, Deokjung Lee[*], Hocheol Shin, "Enriched Burnable Absorbers in PWR Fuel Assembly", KNS Autumn Meeting, Pyeongchang, Korea, October 30-31 (2014).

35. Hyunsuk Lee, **Chidong Kong**, Deokjung Lee[*], "Status of Monte Carlo Code Development at UNIST", PHYSOR2014, Kyoto, Japan, September 28-October 3 (2014).

36. Hyunsuk Lee, **Chidong Kong**, Deokjung Lee[*], "A New Monte Carlo Neutron Transport Code at UNIST", KNS Spring Meeting, Jeju, Korea, May 28-30 (2014).

37. Taewoo Tak, **Chidong Kong**, Jiwon Choe, Deokjung Lee[*], "Reflector Performance Study in Ultra-long Cycle Fast Reactor", KNS Autumn Meeting, Kyeongju, Korea, October 23-25 (2013).

38. Sooyoung Choi, **Chidong Kong**, Deokjung Lee[*], "Status of Deterministic Transport Code Development at UNIST", KNS Autumn Meeting, Kyeongju, Korea, October 23-25 (2013).

39. Hyunsuk Lee, **Chidong Kong**, Sooyoung Choi, Deokjung Lee[*], "Hybrid Method of MOC and MC for Efficient Continuous Energy Neutron Transport Analysis", ANS Annual Meeting, Atlanta, GA, USA, June 16-20 (2013).